This manuscript has been published in EARTH AND PLANETARY SCIENCE LETTERS.

https://doi.org/10.1016/j.epsl.2025.119489

Assessing the timing of deep ocean oxygenation from uranium elemental and isotopic compositions of ophiolites

Joel B. Rodney[a*], Morten B. Andersen[b], Daniel Stubbs[a, c], C. Johan Lissenberg[b], Omar Gianola[d], Matthias Willbold[e], Tim Elliott[a]

[a]Bristol Isotope Group, School of Earth Sciences, University of Bristol, Wills Memorial Building, Queen's Road, Bristol, BS8 1RJ, UK

[b]School of Earth & Environmental Sciences, Cardiff University, Park Place, Cardiff, CF10 3AT, UK

[c]National Nuclear Laboratory, Central Laboratory, Sellafield, Cumbria, UK, CA20 1PG

[d]Department of Geosciences, University of Padova, Via G. Gradenigo 6, 35131 Padova, Italy

[e]Georg-August-Universität Göttingen, Geowissenschaftliches Zentrum Göttingen, Abt. Geochemie und Isotopengeologie, Goldschmidtstr. 1, 37077 Göttingen, Germany

*Corresponding author

Email addresses: joel.rodney@bristol.ac.uk (J.B. Rodney), andersenm1@cardiff.ac.uk (M.B. Andersen), dstubbs95@icloud.com (D. Stubbs), lissenbergcj@cardiff.ac.uk (C. J. Lissenberg), omar.gianola.res@gmail.com (O. Gianola), matthias.willbold@uni-goettingen.de (M. Willbold), tim.elliott@bristol.ac.uk (T. Elliott).

Abstract

The concentration of dissolved oxygen in the deep oceans has varied over Earth History, but the timing of the transition from anoxic to oxic deep oceans is debated. Under modern-day, oxic, deep ocean conditions, alteration of the upper sections of mafic oceanic crust with U-rich seawater leads to U enrichment, low Th/U ratios, and heterogeneous $^{238}U/^{235}U$ ratios relative to fresh mid-ocean ridge basalt (MORB). Given the solubility behaviour of U, its uptake into altered oceanic crust (AOC) is expected to be smaller and less isotopically fractionated when deep oceans were anoxic and thus U-poor. Determining when, in the geological record, the U elemental and isotopic systematics of ancient oceanic crust first resemble modern day AOC should indicate when deep oceans became oxic. We provide U concentration, Th/U, and U isotopic data on upper-crustal sections of three ophiolites from 750 to 480 Ma, spanning the period inferred for deep ocean oxygenation (~ 850 to 400 Ma). The ophiolites at 480 and 540 Ma have high U contents, low Th/U ratios, and variability in $^{238}U/^{235}U$ ratios like modern-day AOC, reflecting seawater alteration of oceanic crust under oxygenated seawater conditions. In contrast, the 750 Ma ophiolite does not show the distinctive decreasing Th/U with increasing U concentrations trend of modern AOC and has fewer samples with $^{238}U/^{235}U$ ratios perturbed from mantle values, reflecting alteration under largely anoxic deep ocean conditions. This is also supported by Fe^{3+}/Fe_T ratios in these samples that are like unaltered modern MORB. Thus, our data suggest oxygenated deep oceans at some time between 750 and 540 Ma, either reflecting a full transition or intermittent deep ocean oxygenation events within an otherwise anoxic deep ocean.

Keywords

Uranium; Seawater alteration; Ophiolites; Altered oceanic crust; Deep Ocean oxygenation

1. Introduction

The evolution of the deep ocean redox state is important for Earth's surface biogeochemical cycles and the evolution of life (e.g., Holland, 1984; Canfield, 1998; Planavsky et al., 2011; Lyons et al., 2014, 2021, 2024 and references therein). Evidence points to the development of an oxic deep ocean in the late Proterozoic – early Phanerozoic (~ 850 to 400 Ma) in response to the rising abundance of oxygen in the atmosphere (Canfield et al., 2007, 2008; Scott et al., 2008; Dahl et al., 2014; Lyons et al., 2014; Sperling et al., 2015; Sahoo et al., 2016; Krause et al., 2018, 2022; Stockey et al., 2024). The atmospheric O_2 abundance needed to oxygenate the deep oceans is uncertain and estimates range from 15 to 50 % of present atmospheric levels (Canfield et al., 2007; Canfield, 2014; Stockey et al., 2024).

Estimates of deep ocean oxygen abundances through the late Proterozoic – early Phanerozoic are largely based on elemental and isotopic proxies (such as C, Fe, U, Mo, Cr, Zn) from sediments on continental shelfs and slopes. Studies on different locations and proxies have often resulted in differing views / timings on when the deep oceans became oxygen rich (e.g., see reviews in Lyons et al., 2014, 2021, 2024; Robbins et al., 2016; Krause et al., 2018, 2022; Mills et al., 2023; Stockey et al., 2024). One potential reconciliation using evidence from multiple proxies is that rather than steady conditions, the deep oceans in this time period likely had considerable variability, with 'brief' (<10 million years) periods of 'ocean oxygenation events', that may have been global or region-specific, against a backdrop of anoxic deep oceans (e.g., Sahoo et al., 2016; Tostevin and Mills, 2020; Krause et al., 2022). For example U isotopic compositions of sediments point towards brief, punctuated levels of deep ocean oxygenation in the Proterozoic, potentially as far back as 1000 Ma (e.g., Wei et al., 2021; Chen et al., 2022; Dang et al., 2022).

However, recent work from Stockey et al. (2024), using global compilations of U and Mo concentrations in shales and marine biogeochemical signals, infer an increase in atmospheric O_2 abundance at the Neoproterozoic – Palaeozoic boundary, but not by enough to oxygenate the deep oceans. Large changes in deep ocean conditions from anoxic / suboxic to more oxic conditions are not inferred until 539 to 400 Ma, with potential full deep ocean oxygenation comparable to modern-day at ~ 420 Ma (Stockey et al., 2024). Many of the proxies used for these estimates however represent local rather than global changes and are largely more representative of the shallower surface level oceans due to being based on sedimentary records. The debate over the timing of this critical change of Earth's surface environment encourages development of new archives of deep ocean conditions and redox-sensitive, elemental and isotopic tracers to probe them.

One novel, potentially more direct proxy of deep ocean redox conditions, is the alteration history of ophiolites. Ophiolites are the remnants of ancient oceanic crust that were subsequently accreted to the continents and thus may preserve a record of deep ocean conditions from their interaction with seawater during alteration. Stolper and Keller (2018) and Stolper et al. (2022) used ophiolites for this purpose by tracking the Fe^{3+}/Fe_T (where Fe_T is total Fe) of their extrusive sections back to 3500 Ma. Circulation of oxygen-rich seawater through oceanic crust oxidises Fe^{2+} to Fe^{3+}, elevating Fe^{3+}/Fe_T. Values above modern unaltered MORB and back arc basin basalts (Fe^{3+}/Fe_T ~ 0.31) indicate the interaction of the ophiolite with oxygen-rich deep ocean waters. The data of Stolper and Keller (2018) and Stolper et al. (2022) suggest that consistently elevated Fe^{3+}/Fe_T are only apparent from the early Phanerozoic and possibly not widespread until late Palaeozoic (<420 Ma).

Other redox sensitive characteristics of altered oceanic crust (AOC) may similarly trace deep ocean oxygenation. A notable feature of the uppermost 500 m of modern AOC is its enrichment in U abundances, by up to an order of magnitude through low temperature interaction with seawater (Hart and Staudigel, 1982; Bach et al., 2003; Kelley et al., 2003). Uranium has two main redox states, reduced and water insoluble U^{4+} and oxidised and water soluble U^{6+} (Langmuir, 1978). After the onset of the first major rise in atmospheric pO_2 across the great oxygenation event (~ 2300 Ma), there would have been a new supply of U^{6+} to the oceans from oxidative continental weathering. However under anoxic marine conditions, the majority of this U would have been reduced and sequestered as U^{4+} complexes into sediments in shallow settings, leading to a low U concentration oceanic reservoir (e.g., Anderson et al., 1989; Klinkhammer and Palmer, 1991; Partin et al., 2013). Only once the oceans became fully oxygenated, would U be present in appreciable abundance in the deep seawater that alters the oceanic crust. Lower U removal rates in ocean basins with decreasing area of anoxic seafloor area, resulted in increasing U concentration of seawater. On the current ocean floor, the enrichment of AOC with seawater U is seen through a clear trend of increasing U concentrations and decreasing Th/U ratios in AOC relative to fresh MORB (Fig. 1a). This trend is seen in multiple sections of modern AOC, with different spreading rates, and modern ophiolites, e.g., Troodos (92 Ma) (Fig. 1a). Thorium is a useful comparison to U due to their similar magmatic behaviours, where both are typically present in the 4+ oxidation state, but different behaviours in the modern, oxidised surface environment, with U being oxidised and water soluble in contrast to Th that is water insoluble. Thorium abundances therefore show little change in the oceanic crust during seawater alteration. The association of high U concentrations with low Th/U ratios in AOC, relative to unaltered MORB, is indicative of U addition from oxygenated seawater to the oceanic crust (Fig. 1a).

The enrichment and redistribution of U in the oceanic crust during oxygenated seawater alteration is also linked to redox sensitive isotopic fractionation that results in AOC having heterogenous $^{238}U/^{235}U$ compositions. Samples of AOC have U isotopic compositions that are both heavier (higher $^{238}U/^{235}U$) and lighter (lower $^{238}U/^{235}U$) than unaltered MORB, as shown from oceanic drill core sites 801C (Pacific), 417/418 (Atlantic), and 1256D (Pacific) (Andersen et al., 2015; Noordmann et al., 2016; Andersen et al., 2024) (Fig. 1b). In the shallowest portions of AOC U addition is dominated by sorption of U^{6+} onto secondary mineral surfaces, such as Fe-oxyhydroxides, which favours lighter U isotopes. In deeper regions of AOC, where conditions become more reducing, seawater transported U^{6+} may undergo partial reduction to U^{4+}, which favours heavier U isotopes, and subsequent incorporation into secondary minerals such as calcite (Andersen et al., 2015, 2024). As the oceanic crust cools and moves off-axis, the overlying sediment package thickness increases, so oxidised seawater flow becomes more restricted, conditions become increasingly reducing and the average $^{238}U/^{235}U$ ratio of AOC increases due to partial reduction processes becoming dominant (Andersen et al., 2024). Some samples of AOC with low Th/U ratios and high U concentrations show $^{238}U/^{235}U$ ratios similar to modern seawater and MORB, likely representing conditions with quantitative U uptake, with little to no net isotopic fractionation (Andersen et al., 2024).

A deep ocean dominated by anoxic conditions, should result in a different behaviour of U during oceanic crust alteration. Firstly, seawater would have a much lower capacity for carrying U into the deep oceans and presumably most would be lost in shelf settings. This would strongly limit the magnitude of elemental U enrichment in AOC. Secondly, the main mechanisms of U incorporation and isotopic fractionation into modern AOC will operate differently under anoxic conditions; in reducing seawater oxic U^{6+} would not be stable and any U uptake into oceanic crust would occur with more quantitative U^{4+} uptake, resulting in limited

isotopic variability in AOC. Thus, identifying when in geological history AOC first shows notable U enrichment (with associated low Th/U ratios), and isotopic variability in U should indicate the onset of oxygen-rich deep oceans.

We apply these U elemental and isotopic proxies using measurements of ophiolite samples. We measure the U concentration, Th/U ratio, and natural U isotopic variations in sample sets from three ophiolites: 750 Ma Gabal Gerf, North Africa (Zimmer et al., 1995), 540 Ma Khantaishir, Mongolia (Gianola et al., 2019), and 480 Ma Annieopsquotch, Canada (Lissenberg et al., 2005), which span the time range suggested for the onset of deep ocean oxygenation.

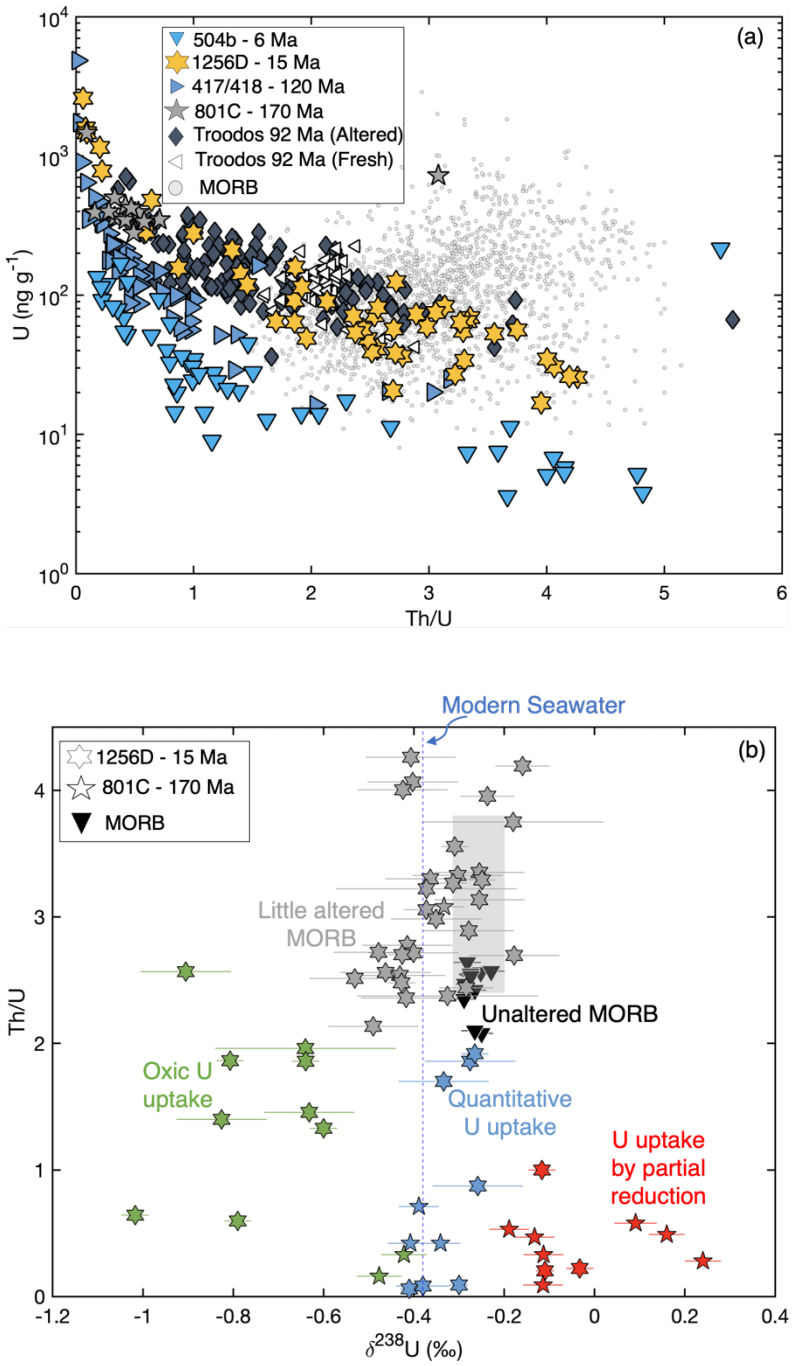

Fig. 1. (a) U concentration vs. Th/U ratio for AOC samples from the modern ocean floor: DSPD / ODP holes 504b (~ 6 Ma) (Bach et al., 2003), 1256D (~ 15 Ma) (Andersen et al., 2024), 417/418 (~ 120 Ma) (Seyedali et al., 2021), 801C (~ 170 Ma) (Andersen et al., 2015). Also shown are data for fresh (Regelous et al., 2014) and altered (Gillis et al., 2015) Troodos ophiolite (92 Ma) samples, and global MORB using a compilation of ICP-MS analyses from

Gale et al. (2013). (b) Th/U ratio vs. $\delta^{238}U$ for AOC samples from the modern ocean floor. Modern seawater composition (Kipp et al. 2022) is shown as a vertical blue dashed line. Grey shaded region represents the average Th/U of normal MORB ± 1 SD using a compilation of ICP-MS analyses from Gale et al. (2013), and the range in $\delta^{238}U$ for MORB (Andersen et al., 2015). Grey data points are samples that are closest in composition to fresh unaltered MORB (black, inverted triangles). Samples with lower Th/U imply U uptake during alteration but under different redox conditions: green data points are samples that are isotopically light (oxic U^{6+} adsorption), blue data points are samples that are similar to MORB or seawater in $\delta^{238}U$ and indicate quantitative U uptake, red data points are samples that are isotopically heavy (partial reduction of U^{6+} to U^{4+} and uptake). Note that DSDP site 417/418 (Noordmann et al., 2016) also has data for $\delta^{238}U$, however there are no associated Th/U values, so these samples are excluded from this figure. Error bars on $\delta^{238}U$ are 2SE.

2. Geological location and samples

The Annieopsquotch ophiolite, 480 Ma (U/Pb zircon age) (Dunning and Krogh, 1985) in Newfoundland, Canada is a 5.5 km thick section of oceanic crust, comprising gabbro, sheeted dykes, and basaltic pillow lavas, with hydrous mineralogical assemblages formed by seawater alteration (Lissenberg et al., 2005). Evidence of this includes dykes crosscutting hydrothermal alteration veins (Lissenberg et al., 2004) and a set of late-stage, off-axis dykes that crosscut the ophiolite stratigraphy that are markedly fresher than the host rocks (Lissenberg et al., 2005); neither would be the case if alteration occurred syn- or post-obduction as a metamorphic overprint (Lissenberg et al., 2005). The Annieopsquotch ophiolite formed following subduction initiation in the Iapetus Ocean and was accreted to the Laurentian continental margin within 10 Myr of formation (Lissenberg et al., 2005). Samples analysed in this work are from the sheeted dyke and extrusive sections.

The Khantaishir ophiolite in Western Mongolia, part of the Central Asian orogenic belt, is divided into the Naran and Taishir massifs, both with exposed mantle sections, overlain by gabbro, sill and dyke complexes, and pillow lavas. These have experienced limited greenschist-facies metamorphism that is either ocean floor or accretion related (Gianola et al., 2019) (with ocean floor alteration being favoured, see below). Reported ages for the Khantaishir ophiolite vary, with Sm-Nd ages of 532 ±40 Ma for the Taishir massif and 540 ±12 Ma for the Naran massif (Gianola et al., 2019), while U/Pb dating of plagiogranites suggests ages of 573 ±8 Ma and 566 ±7 Ma (Jian et al., 2014). Gianola et al., (2019) estimate an age range of ~ 550 – 530 Ma, and for this study, we use an average age of 540 Ma. Dating of metamorphic zircons from a shear zone at the ophiolite's boundary with the microcontinent it accreted to suggest

obduction occurred at 514 ±8 Ma (Jian et al., 2014). Samples analysed here span the gabbro, sill and dyke complex, and extrusive section.

The Gabal Gerf ophiolite, located in the Southern Eastern Desert of Egypt and Red Sea Hills of Sudan, is part of the Arabian-Nubian shield (Zimmer et al., 1995). It consists of the Gabal Gerf, Gabal Harga Zarga, and Gabal Heiani nappe complexes, which include, a serpentinised ultramafic melange, serpentinised or carbonated ultramafics, gabbro, sheeted dykes, and basaltic pillow lavas which have variably experienced up to greenschist-facies metamorphism (Zimmer et al., 1995). Pooled Sm-Nd ages suggest a mean age of ~ 750 Ma for gabbro crystallisation (Zimmer et al., 1995), with obduction occurring around ~ 715 Ma (Kröner et al., 1992). Samples analysed in this work cover ultramafic cumulates, gabbro, sheeted dyke complexes, and pillow lavas.

Many ophiolites are formed in suprasubduction zone environments, which may result in lower Th/U ratios and higher U concentrations than MORB, as seen in fresh glass samples from the Troodos ophiolite (Fig. 1a). However, these fresh samples do not show such marked enrichment in U concentration and low Th/U as most of their altered counterparts (Fig. 1a). Therefore, we emphasise that the tectonic setting of oceanic crust for each ophiolite has a minor influence on the magnitude of U enrichment, relative to the effect of seafloor alteration that dominates over any primary differences (Fig. 1a). Details on the tectonic settings of each ophiolite are, however, provided in Supplementary Material Section 1.

A full comparison of alteration mineralogy in modern AOC and our samples is beyond the scope of this work, but details can be found in other studies (e.g., Alt and Honnorez, 1984; Zimmer et al., 1995; Alt and Teagle, 2003; Lissenberg et al., 2004, 2005; Alt et al., 2010;

Gianola et al., 2019). However, we provide some descriptions and representative petrographic images illustrating the typical mineralogy of submarine alteration evident in the ophiolite samples in Supplementary Material: Section 1. In brief, low temperature alteration phases (e.g., celadonite, saponite, and prehnite), variations in mineralogy with seafloor temperature gradient (celadonite in extrusive section samples and calcite and epidote in deeper dyke samples), and primary igneous textures (e.g., ophitic and pilotassitic textures) are evident in Annieopsquotch and Khantaishir ophiolite samples (Fig. S2). This, in conjunction with field observations given above, indicate that the ophiolites preserve seafloor alteration characteristics rather than metamorphic overprints syn- or post-obduction. It is important to note that while the samples studied in this work were dominantly collected to study magmatic processes, and so the most seawater altered samples may have been systematically avoided, the alteration mineralogy identified and differences between more altered (Fig. S2a-e) and fresher samples (Fig. S2f), indicates heterogeneous alteration of samples, as would be expected from seawater alteration. We therefore consider our samples to be representative of submarine alteration of *in-situ* oceanic crust. Unfortunately, no thin sections were available for the Gabel Gerf samples.

3. Methods

Major and trace element data for the ophiolite samples are reported in Zimmer et al. (1995), Lissenberg et al. (2005), and Gianola et al. (2019). For measurement of Th and U concentrations (non-isotope dilution) 50 mg of sample powders were dissolved and analysed on a ThermoFinnigan Element2 at the Bristol Isotope Group laboratories following Andersen et al. (2014). Measured reference materials are in good agreement with reference values (Supplementary Material: Section 2).

Uranium isotopic measurement, sample preparation and analysis followed Andersen et al. (2015), detailed fully in Supplementary Material: Section 2. Uranium isotope analysis was conducted in the University of Bristol Isotope Group laboratories. Approximately 0.5 – 3 g of sample powder, spiked with the IRMM3636 ^{236}U – ^{233}U double spike (Richter et al., 2008), was dissolved. Purification and U separation used a two-column method, with TRU resin followed by UTEVA resin. Uranium aliquots were dissolved in 0.2 M HCl (aiming for U concentrations of 50 – 300 ng g^{-1}) for isotopic analysis. Procedural blanks were <30 pg U, negligible compared to amount of U consumed per measurement, ~ 15 – 80 ng.

Uranium isotope compositions were measured on a ThermoFinnigan Neptune MC-ICP-MS (serial no. 1002) in low mass resolution (M/ΔM ~ 2000, 5 to 95 % peak height definition). Samples were bracketed by measurements of the double-spiked standard CRM-145. Uranium isotope ratios for $^{238}U/^{235}U$ and $^{234}U/^{238}U$ were calculated using the exponential mass fractionation law and reference double spike $^{233}U/^{236}U$ ratio (Richter et al., 2008). Data are reported in δ notation with $\delta^{238}U = [(^{238}U/^{235}U_{Sample} / {}^{238}U/^{235}U_{CRM\text{-}145}) - 1]$ and $\delta^{234}U = [(^{234}U/^{238}U_{Sample} / (^{234}U/^{238}U_{CRM\text{-}145}/ (1–0.0386)) - 1]$. Note that $\delta^{234}U$ values are reported

relative to secular equilibrium, given the CRM-145 standard has a $\delta^{234}U$ of −38.6 ‰ relative to secular equilibrium (Cheng et al., 2013).

Long term external reproducibility at various measured U intensities has been estimated using aliquots of the well characterised reference material BHVO-2 measured during different analytical sessions. The external reproducibility of $\delta^{238}U$ and $\delta^{234}U$ for BHVO-2 ranges from ±0.09 – 0.03 ‰, 2SD, and ±4 – 0.9 ‰, 2SD, respectively, for measured ^{238}U intensities of 200 – 1000 pA respectively (full details reported in Supplementary Material: Section 2). Uranium isotopic measurements of international reference materials analysed (BHVO-2, BCR-2, BIR, W-2A, and CZ1) agree with literature values (Supplementary Material: Section 2).

4. Results

Uranium isotopic compositions, concentrations, and Th/U ratios are reported in Supplementary Material: Section 3 and table S3. To present a homogeneous dataset, we exclude from further discussion: 1) samples measured for Th/U ratios, but not U isotopic compositions and 2) amphibolites and ultramafic / peridotite samples that have undergone serpentinization from Gabel Gerf, given these lithologies are not represented in the other ophiolites, Moreover, Pavia et al. (2023) illustrated the latter are sensitive to post-serpentinization weathering processes in subaerial environments that question their utility as palaeo-seawater archives.

Some samples from Annieopsquotch (480 Ma) and Khantaishir (540 Ma) show enrichment in U relative to Th, with high U concentrations and low Th/U ratios relative to the field defined by MORB (Fig. 2a, b). This trend of simple U-addition is similar to that seen in modern sections of AOC the Troodos ophiolite (Fig. 2b). In figures, we highlight the samples that plot on this vector of U enrichment relative to modern MORB associated with decreasing Th/U ratios, as observed in AOC in the current ocean basins. Such samples are identified as having Th/U ratios lower than one standard deviation of average MORB Th/U from spreading centres and back arc settings, i.e., a Th/U ratio <2.4, using a compilation of ICP-MS analyses from Gale et al. (2013), and U concentrations above 55 ng g^{-1}, the average concentration of depleted MORB from Gale et al. (2013). Nine samples from Khantaishir and five from Annieopsquotch pass these criteria and define a similar array to data from modern AOC and altered Troodos ophiolite samples (Fig. 2a & b). In contrast, Gabel Gerf (750 Ma) samples, which generally have lower Th concentrations (Fig. 2a), have low Th/U ratios in samples that also have low U concentrations (Fig. 2b).

Samples from all three ophiolites have $\delta^{238}U$ that overlap with MORB (Fig. 2c). However, samples with low Th/U ratios from Annieopsquotch and Khantaishir, and a single sample from Gabel Gerf, have $\delta^{238}U$ lower than fresh MORB, similar to modern AOC (Andersen et al., 2015, 2024). There are no $\delta^{238}U$ measurements, outside of uncertainty, higher than the field of modern MORB (Fig. 2c).

Samples from all ophiolites show variation in $\delta^{234}U$ with compositions above and below secular equilibrium, where secular equilibrium is $\delta^{234}U = 0$ (Fig. 3). However, most samples have $\delta^{234}U$ >0 and extend up to ~ +442 ‰, above modern seawater (145.6 ±0.3 ‰, 2SE; Kipp et al., 2022). There are no clear correlations between $\delta^{234}U$ and $\delta^{238}U$ or U concentrations (Fig. 3a & b) or Th/U ratios (Fig. S4). In general, however, samples with the lowest U concentrations tend to have the greatest deviation in $\delta^{234}U$ from secular equilibrium (Fig. 3b). This overview excludes the anomalous Khantaishir sample with the highest $\delta^{234}U$ (~ +442 ‰) that also has a high U concentration (~ 183 ng g^{-1}), marked with a cross on figures 2 and 3.

Figures 2 and 3 distinguish samples by lithology, which provides a coarse index of depth within the ophiolite stratigraphy. Samples with the highest U concentrations and values of $\delta^{238}U$ lower than MORB are predominantly, but not exclusively, from the extrusive sections of ophiolites (Fig. S5). This also argues against post-obduction alteration of samples, which would result in all sections showing similar degrees of alteration.

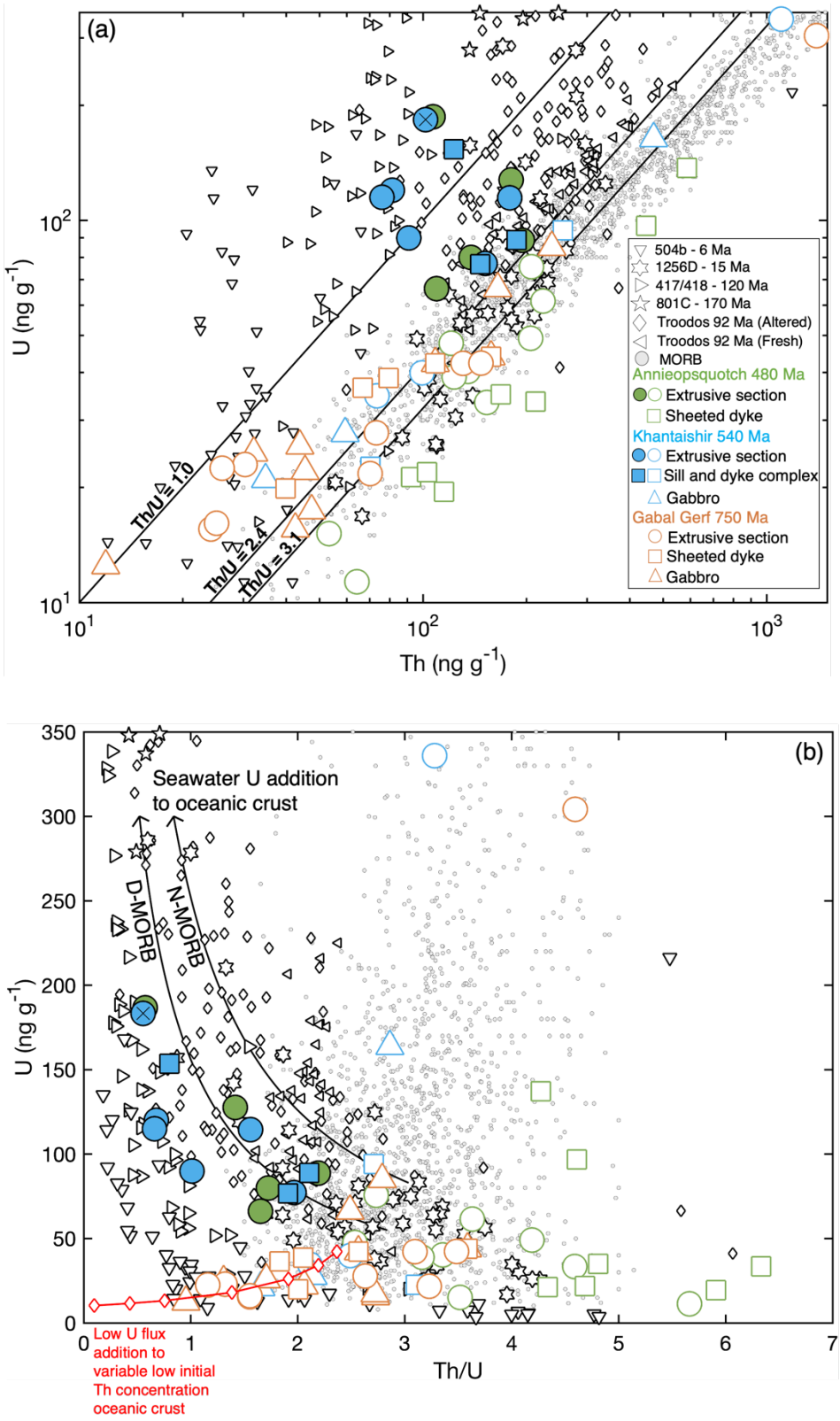
(a)
U (ng g-1)
Th (ng g-1)
Th/U = 1.0
Th/U = 2.4
Th/U = 3.1
504b - 6 Ma
1256D - 15 Ma
417/418 - 120 Ma
801C - 170 Ma
Troodos 92 Ma (Altered)
Troodos 92 Ma (Fresh)
MORB
Annieopsquotch 480 Ma
Extrusive section
Sheeted dyke
Khantaishir 540 Ma
Extrusive section
Sill and dyke complex
Gabbro
Gabal Gerf 750 Ma
Extrusive section
Sheeted dyke
Gabbro
(b)
Seawater U addition
to oceanic crust
D-MORB
N-MORB
U (ng g-1)
Th/U
Low U flux
addition to
variable low initial
Th concentration
oceanic crust

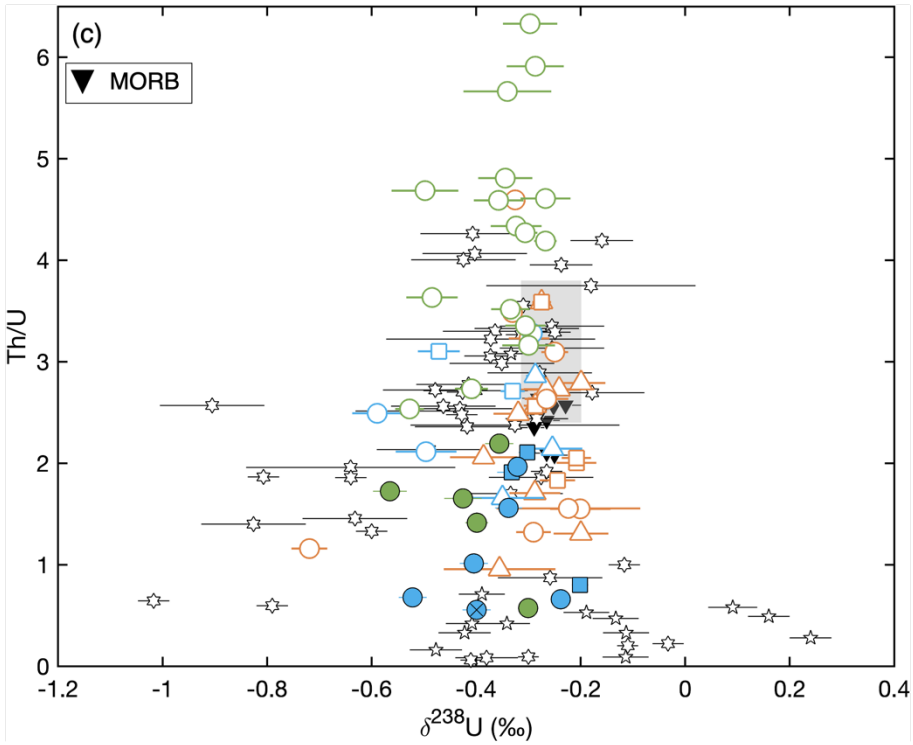

Fig. 2. (a) U concentration vs. Th concentration, (b) U concentration vs. Th/U ratio and (c) Th/U ratio vs. $\delta^{238}U$ for ophiolite samples, modern sections of AOC, the Troodos ophiolite, and MORB. Symbols are the same as in figure 1. Ophiolite data are grouped into lithology of samples, circles are samples from the extrusive section, squares are sheeted dykes / sill and dykes, and triangles are gabbros. Green samples are from Annieopsquotch, blue from Khantaishir, and orange from Gabal Gerf. Ophiolite samples are grouped into two sets, those that plot on a vector of U addition to MORB and have increasing U concentration and decreasing Th/U indicative of U addition from typical MORB compositions (filled symbols) and those that do not (hollow symbols), see (b) and main text for details. The Khantaishir sample with the highest $\delta^{234}U$ (Fig. 3a) is marked with a cross. In (a) three lines of constant Th/U, 3.1 (average MORB), 2.4, and 1 are shown. Note that

the concentrations are on a log scale and have been cut at concentrations of Th 1500 ng g^{-1} and U 350 ng g^{-1}. In (b) two representative mixing curves (black lines) show the effect of simple U addition to a normal and depleted MORB starting composition from Gale et al. (2013). Also, in (b) the red line denotes oceanic crust compositions with variable low initial Th concentrations (white diamonds at 100, 75, 50, 25, 10, 5, and 1 ng g^{-1} Th) and constant Th/U ratio of 3.1 that has been perturbed by a representative equal amount of a low U flux, 10 ng g^{-1}. In (c) Error bars on $\delta^{238}U$ are 2SE.

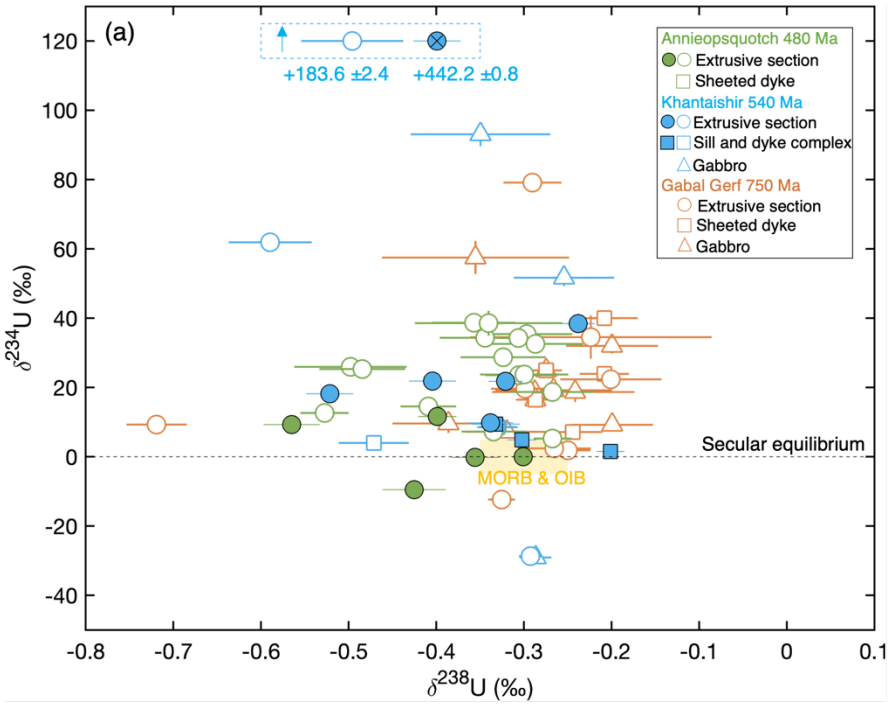
(a)
+183.6 ±2.4
+442.2 ±0.8
Annieopsquotch 480 Ma
Extrusive section
Sheeted dyke
Khantaishir 540 Ma
Extrusive section
Sill and dyke complex
Gabbro
Gabal Gerf 750 Ma
Extrusive section
Sheeted dyke
Gabbro
Secular equilibrium
MORB & OIB
δ234U (‰)
δ238U (‰)

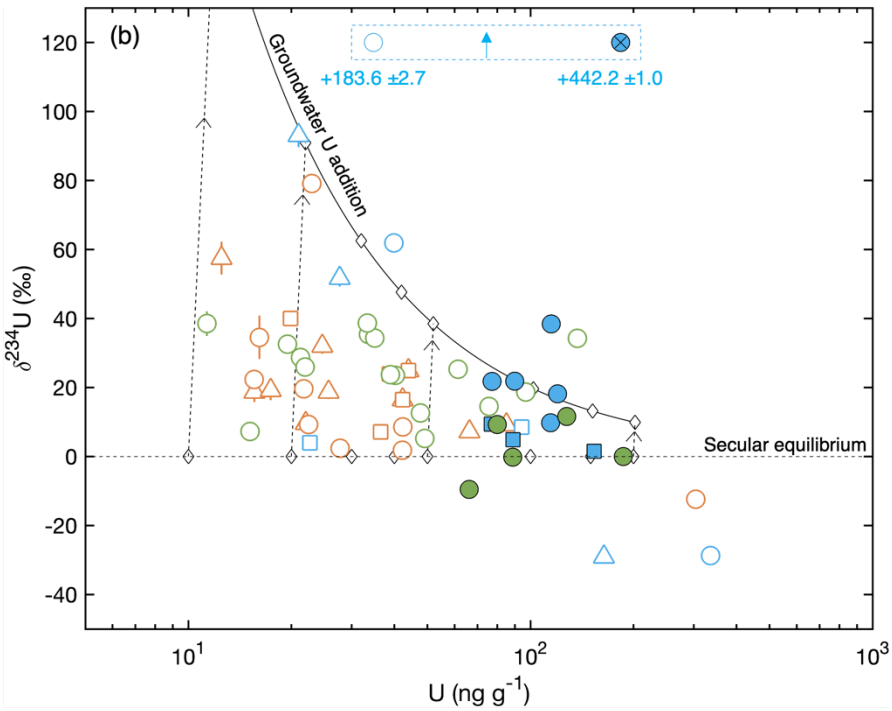
(b)
Groundwater U addition
+183.6 ±2.7
+442.2 ±1.0
Secular equilibrium
δ234U (‰)
U (ng g-1)

Fig. 3. (a) $\delta^{234}U$ vs. $\delta^{238}U$ and (b) $\delta^{234}U$ vs. U concentration for ophiolite samples. Dashed black line at $\delta^{234}U = 0$ represents secular equilibrium. Ophiolite sample symbol groupings shapes, and colours are the same as in figure 2. Samples from Khantaishir circled in the dashed blue box plot off the scale in $\delta^{234}U$ (Table S3). In (a) the yellow shaded region is the range of $\delta^{234}U$ and $\delta^{238}U$ represented by MORB and ocean island basalt (OIB) samples from Andersen et al., (2015). In (b) the result of addition of a constant flux of groundwater U (2 ng g^{-1} with $\delta^{234}U = 1000$ ‰) to samples in secular equilibrium, with a range of initial U concentrations, is shown as the solid black curved line. Vectors of alteration (dashed lines) link specific fresh and altered hypothetical samples (white diamonds) with initial U concentrations (10, 20, 30, 40, 50, 100, 150, and 200 ng g^{-1}). Note that in (b) the U concentration is plotted on a log scale. Error bars are 2SE.

5. Discussion

5.1 Secular equilibrium and sample alteration

The U budgets of ophiolites represent the primary rock inventory with additions from ancient seafloor alteration and possibly more recent subaerial exposure. Measurements of $\delta^{234}U$ can help differentiate these processes. A deviation from secular equilibrium ($\delta^{234}U = 0$) suggests U loss or gain in the last ~ 2 Myr. Uranium loss during chemical weathering typically causes ^{234}U deficits ($\delta^{234}U < 0$) through preferential loss of daughter ^{234}U atoms that sit in damaged recoil sites (Thurber, 1962; Bacon, 1978; MacDougall et al., 1979; Chabaux et al., 2003; Gaschnig et al., 2021) resulting in complementary $\delta^{234}U > 0$ of decreasing magnitude in groundwaters, rivers, and oceans (e.g., Osmond and Cowart, 1976; Dunk et al., 2002; Kipp et al., 2022).

Many samples measured across all three ophiolites, have $\delta^{234}U$ higher than secular equilibrium, implying some recent U gain. In subsurface aqueous environments equilibrium adsorption-desorption exchange between ionic U^{6+} complexed species in the groundwater and mineral surfaces can lead to net adsorptive U uptake (e.g., Osmond and Cowart, 1976; Sylwester et al., 2000). The extreme $\delta^{234}U$ of groundwater, typically ~ 50 – 1000 ‰ (extending to >2000 ‰) (Osmond and Cowart, 1976), means samples can acquire modestly perturbed $\delta^{234}U$ (~ 20 ‰) with only minor elemental U addition. We illustrate this in figure 3b where hypothetical samples with a range of initial U concentrations (white diamonds at secular equilibrium) are perturbed by a fixed addition of groundwater U (2 ng g^{-1} with a characteristic $\delta^{234}U$ value of 1000 ‰). This yields the black curve (perturbed samples shown as white diamonds along this curve, which are shifted imperceptibly along the x-axis i.e., minor total U addition) that reproduces much of the variability seen in $\delta^{234}U$, including the tendency for samples with lower

U concentration to have higher $\delta^{234}U$. For samples with U concentrations over 20 ng g^{-1} this flux would account for <10 % of the U content of samples, this would result in a small shift in U concentrations. We also, following the approach in Andersen et al. (2024), model the changes in Th/U ratios (Fig. S6a) and $\delta^{238}U$ (Fig. S6b & c) following groundwater U addition with $\delta^{234}U$ = 1000 ‰ (Supplementary Material: Section 4). In brief shifts in Th/U and $\delta^{238}U$ are calculated and to account for unknown $\delta^{238}U$ compositions of groundwater we model two scenarios using the lowest and highest $\delta^{238}U$ compositions in each ophiolite for the groundwater composition. We assume starting $\delta^{234}U$ compositions of 0 ‰ for the rock with no groundwater U addition and apply the model to samples with $\delta^{234}U \geq 0$ ‰. Samples plot within uncertainty of a 1:1 line between corrected compositions for groundwater U addition and the measured compositions in Th/U and $\delta^{238}U$ (Fig. S6), except for the sample from Khantaishir with highest $\delta^{234}U$ (~ 44 % groundwater U addition, Table S4). This sample, however, when corrected for recent U addition still shows evidence of seawater U addition, i.e., low Th/U (measured Th/U 0.6 versus corrected Th/U 1.0). This simple model highlights that recent subaerial weathering may not have a significant impact on Th/U and $\delta^{238}U$ compositions, even when showing elevated $\delta^{234}U$.

An important observation is also that samples with high U concentrations are not systematically associated with elevated $\delta^{234}U$. This indicates that alteration during recent ophiolite exposure is not the main cause of their U enrichment relative to MORB. The $\delta^{234}U$ isotopic data however only preserve the last ~ 2 Myr of groundwater interaction and therefore do not reflect the entire history of potential groundwater U addition that may have occurred over longer timescales. As discussed above, however, other lines of evidence, such as the alteration mineralogy of samples indicating seafloor alteration assemblages rather than subaerially formed secondary minerals, support the inference of limited groundwater U addition to the samples.

Furthermore, there is no obvious relationship between $\delta^{234}U$ and $\delta^{238}U$ (Fig. 3a). Much of the range of $\delta^{234}U$ is found in samples with $\delta^{238}U$ within uncertainty of primary magmatic $\delta^{238}U$ (Fig. 3a). This supports the notion developed above that modest perturbation of $\delta^{234}U$ by groundwaters with high $\delta^{234}U$ need not dramatically alter the overall U budget, especially for samples with high U concentrations from submarine alteration acquired before such subaerial weathering (Fig. S6). The low U concentrations of groundwater (e.g., Dunk et al., 2002) results in only minor amounts of U addition compared to the greater quantities of U that may be added by larger volumes of U-rich seawater during seafloor alteration. Therefore, our samples may have experienced recent subaerial groundwater U addition, but, and especially for samples with high U concentrations, this would not result in significant changes in U elemental and isotopic compositions, although larger changes may occur in low U concentration samples. We therefore focus our interpretations on high U concentration samples with low Th/U ratios that are most indicative of compositions resulting from seafloor alteration.

5.2 Comparisons of ophiolites to more recent altered oceanic crust

Our analyses show distinct patterns of U enrichment in the two younger ophiolites relative to the oldest one. In the former, most samples with high U concentrations plot on a vector of increasing U concentration and decreasing Th/U ratio, similar to modern AOC (Fig. 2b). This trend is readily explained by the process of U addition during seafloor alteration, which we depict on figure 2b (Hart and Staudigel, 1982; Bach et al., 2003; Kelley et al., 2003; Andersen et al., 2015, 2024). Some Annieopsquotch samples extend to high Th/U ratios (>4.5) at low U concentrations (Fig. 2a, b) which may indicate some U loss and or remobilisation as seen in some deeper sections of modern AOC (Andersen et al., 2024).

Samples from the older Gabel Gerf ophiolite also have Th/U ratios lower than unaltered MORB, but in samples with the lowest rather than the highest U concentrations (Fig. 2b). They define a group with low Th and U concentrations, distinct from the Khantaishir and Annieopsquotch samples that show significant U enrichment similar to modern seafloor samples (Fig. 2a). The variable but low Th/U ratios in Gabal Gerf likely reflect the addition of small amounts of seawater or recent groundwater U to oceanic crust with low initial Th concentrations (Fig. 2a & b), orders of magnitude smaller than that observed in Khantaishir, Annieopsquotch, and modern AOC. We reproduce these Gabel Gerf samples with a simple model that starts with a range of unaltered crustal compositions with variable, low initial Th concentrations (1, 5, 10, 25, 50, 75, and 100 ng g^{-1}) but constant Th/U ratios (3.1). A fixed, low U flux (10 ng g^{-1}) added to these model compositions successfully accounts for the trend displayed by the Gabal Gerf and some Khantaishir samples, that have low Th/U ratios (Fig. 2b) and low Th and U concentrations (Fig. 2a). There are no Gabel Gerf samples that plot on vector of seawater U addition to oceanic crust, with low Th/U ratios at high U concentrations (Fig. 2b). The systematics of U and Th trends identified in the Gabal Gerf samples are therefore not characteristic of seawater alteration on the modern, oxic ocean floor. They are more readily attributed to minor U addition, from either groundwater of perhaps more simply, from seafloor alteration in an anoxic ocean. The Gabal Gerf data therefore suggest that the redox state of the deep oceans was different at ~ 750 Ma relative to 540 and 480 Ma.

The contrast in the $\delta^{238}U$ between the oldest and more recent ophiolites is more subtle than the contrast in U concentrations and Th/U ratios. All analyses of Gabel Gerf, bar one sample, are within error of modern magmatic $\delta^{238}U$ (Fig. 2c). As argued above, the low Th/U ratio in some Gabel Gerf samples reflect minor U addition to low Th concentration samples. This process

appears to result in perturbed $\delta^{238}U$ in only one case, with this sample also having a low U concentration (Fig. S5) and may be related to recent groundwater U addition. All other Gabal Gerf samples reflect the unfractionated bulk addition of minor amounts of U, which we attribute to this process occurring in an anoxic ocean. In contrast, $\delta^{238}U$ in some low Th/U ratio samples from both Khantaishir and Annieopsquotch are significantly lower than unaltered modern MORB (Fig. 2c), which we interpret as further evidence of oxic submarine alteration. This is a less definitive signature than the U-Th elemental systematics, as different styles of ^{238}U-^{235}U fractionation are observed with depth in modern AOC (Andersen et al., 2015, 2024). In keeping, some of the low Th/U ratio samples from Khantaishir and Annieopsquotch have $\delta^{238}U$ within uncertainty of unaltered MORB, likely reflecting near-quantitative U addition during seafloor alteration.

It is notable that there are no $\delta^{238}U$ compositions outside of uncertainty in the ophiolite samples higher than unaltered MORB, as can occur through partial reduction of U^{6+} (Fig. 1b). Altered oceanic crust may develop high $\delta^{238}U$ from more restrictive U addition due to sediment build up off-axis restricting the flow of oxidised seawater through the oceanic crust. Conditions of alteration therefore can become more reducing with age of oceanic crust, resulting in higher $\delta^{238}U$, as seen in some modern AOC, most notably from the oldest AOC samples (Hole 801, Fig. 1b) (Andersen et al., 2015, 2024). Our U enriched ophiolite samples may not have been on the seafloor for long enough before obduction for conditions of alteration to become dominantly reducing. As seen in hole 1256D (~ 15 Ma) the majority of samples have low $\delta^{238}U$ values, with high $\delta^{238}U$ only seen in a few samples at select horizons (Andersen et al., 2024). Therefore, it is perhaps expected that most samples from AOC altered in an oxic deep ocean analysed will have predominantly low $\delta^{238}U$ as is seen in Annieopsquotch and Khantaishir ophiolite samples. Whether $\delta^{238}U$ values of AOC are higher or lower than MORB, our

conclusions remain unchanged, as both require that U^{6+} is present in the oxic deep oceans. The $\delta^{238}U$ data therefore corroborates with the inference from the elemental U and Th systematics of changing styles of submarine alteration from anoxic at 750 Ma to oxic at 540 and 480 Ma.

Comparisons of ophiolite samples with modern AOC are potentially affected by sampling biases, as ophiolite samples are typically collected to study magmatic processes and so the most seawater altered samples may be avoided. This could explain some of the more muted levels of U enrichment seen in our samples from Khantaishir and Annieopsquotch and the lack of enrichment seen in Gabal Gerf. In this context we note that our interpretation of Gabal Gerf as altered in anoxic deep ocean conditions is a conservative interpretation. If the lack of U enrichment at Gabal Gerf were solely due to a sample bias, then it would extend our inferred duration of oxic deep ocean conditions considerably further back in time than most current estimates (see section 1 and 5.3). Thus, the lack of U enrichment in Gabal Gerf is unsurprising. More significant is the evidence for U addition in Khantaishir samples, indicative of oxic deep oceans at 540 Ma, also older than many literature estimates.

5.3 Comparison with other recent models of changing ocean anoxia

Given the use of ocean crust alteration recorded in ophiolites in this study, it is valuable to compare our observations to the estimates of deep ocean dissolved O_2 concentrations derived from Fe^{3+}/Fe_T ratios in ophiolites (Stolper and Keller 2018). Stolper and Keller (2018) calculate a gradual increase in the dissolved O_2 concentration of the deep ocean from anoxic conditions in the Neoproterozoic (a period encompassing the Gabel Gerf ophiolite) to values resolvable from zero in the early Palaeozoic (during which Annieopsquotch and Khantaishir were formed and altered), with subsequent continued rise to modern day concentrations (Fig. S7a). We note

that the Fe^{3+}/Fe_T ratios of Gabal Gerf samples are amongst the most reduced values in the Neoproterozoic time step of Stolper and Keller (Fig. S7b) and Fe^{3+}/Fe_T in Gabal Gerf samples show no correlation with $\delta^{238}U$ (Fig. S8). Unfortunately, we do not have Fe^{3+}/Fe_T data for our Annieopsquotch or Khantaishir samples.

The systematic change in style of seawater U addition between ophiolites of different ages in our study is, at least qualitatively, consistent with the timing of onset of discernible deep ocean oxygenation inferred by Stolper and Keller (2018). However, their model does not show a significant rise in deep ocean O_2 concentrations until ~ 420 Ma, which is younger than the formation and obduction of our youngest ophiolite (480 Ma) which we infer to have experienced alteration in an oxygenated deep ocean. In a subsequent, more detailed study of the Bay of Island ophiolite (485 Ma) Stolper et al. (2022) infer, from Fe^{3+}/Fe_T ratios, oxidation of volcanic rocks in the ophiolite sequence, but to less of an extent than seen in the late Palaeozoic-modern systems. Stolper et al. (2022) argue that, from globally binned averages, the clear increase in deep ocean O_2 is not seen until the late Palaeozoic. However, with individual locations (e.g., Bay of Island, Annieopsquotch, Khantaishir), increases in deep ocean O_2 can be seen earlier, which may represent a global trend or local / transient events in deep ocean O_2 levels. It is encouraging that Annieopsquotch and the Bay of Island ophiolite, both of similar ages and from similar palaeo-geographic locations show evidence of increased deep ocean O_2 from different palaeo-redox proxies.

Perfect agreement between the two proxies is not expected however, as the controls on Fe oxidation and U addition through seawater interaction are different and redox thresholds between the systems may be different. The main host minerals and sites for U in AOC are poorly constrained and U addition may be associated with multiple phases of secondary

mineral formation in oxidising and reducing conditions. Increases in Fe^{3+}/Fe_T ratios however, that may scale with increasing levels of deep ocean O_2, will primarily be associated with phases such as Fe-oxyhydroxides that may overprint earlier alteration phases (Alt, 2004). Uranium addition to AOC, which may not directly scale with increasing levels of deep ocean O_2, may be more sensitive to low levels of dissolved O_2 than Fe^{3+}/Fe_T ratios. Different elemental systems have different thermodynamic redox thresholds, however, the exact redox potential for each element will vary as a function of the local chemical and physical conditions (e.g., pH and ligand-complexation) and lithology investigated (Langmuir, 1978; Anderson et al., 1989; Algeo and Li, 2020). Therefore, the measurable fingerprint of deep ocean oxygenation may differ for the U and Fe system during seafloor alteration in AOC. Our U data could record lower levels of deep ocean oxygenation than recorded by the Fe system (Stolper and Keller, 2018; Stolper et al., 2022), thus providing a potential explanation for the different time inferences from the proxies. Overall, however we stress that it is difficult to envisage the extensive addition of U to the oceanic crust, which we observe in 480 and 540 Ma ophiolites, without high U concentration in deep ocean water, which requires an oxygenated deep ocean.

Sedimentary records have also been analysed to investigate deep ocean O_2 (see section 1) and the marked rise in U content in some marine sedimentary sections at ~ 600 Ma (e.g., Partin et al., 2013) has been interpreted to reflect the timing of deep ocean oxygenation, similar to the timing based on arguments from the diversification of life (e.g., Butterfield, 2007; Canfield et al., 2007; Dahl et al., 2010; Lenton et al., 2014; Planavsky et al., 2014). However, a recent compilation of marine sedimentary U and Mo concentration data, suggests no major change in the oxygen content of the deep oceans until ~ 420 – 400 Ma (Stockey et al., 2024). This timing again is significantly later than our inference of deep ocean oxygenation >540 Ma.

A possible explanation of the different inferred timing of deep ocean oxygenation is that the approaches have a different sensitivity to transient ocean oxygenation events, i.e., brief periods of increased ocean oxygenation against a backdrop of long term ocean anoxia. Marine sedimentary data integrates over ~ 10-million-year timescales, and as such, may not capture transitory ocean oxygenation events. Although ophiolites also integrate conditions on the deep ocean floor over a similar timescale, a signature of U addition from a short-lived period of oxygenation can be seen as an elevated U concentration or low Th/U ratio relative to a baseline of unaltered MORB. In the sedimentary case, short-lived periods of oxygenation, that result in spikes in U concentrations relative to average compositions, may be damped by the averaging effect of continuous sedimentation. Thus, it may be that the U ophiolite proxy is better at capturing shorter ocean oxygenation events in an otherwise anoxic deep ocean.

However, ophiolites provide a direct record of interaction between basaltic rock and deep ocean water, while sedimentary proxies of ocean anoxia trace local conditions on continental shelves and the consequences of these observations for deep ocean conditions requires further biogeochemical modelling. It is interesting to note that the raw sediment U concentration data in the study of Stockey et al. (2024, their supplementary Fig. S2) show a systematic increase in the 75th percentile and maximum value in temporally binned samples younger than ~ 550 Ma. Only with a more sophisticated, statistical learning treatment, to address sample bias, is the rise in sedimentary U content (used to model oxygenation of the deep ocean) delayed until ~ 420 – 400 Ma.

6. Conclusions

Mafic samples from the Annieopsquotch (480 Ma) and Khantaishir (540 Ma) ophiolites showing a trend between low Th/U ratios, <2.4, and high U concentrations, >55 ng g^{-1}, and variability in $\delta^{238}U$, ranging from –0.5 to –0.2 ‰, reflect the significant uptake of U during seafloor alteration prior to obduction. These observations imply alteration by oxic, deep ocean water, with U present in its oxidised form, since at least 540 Ma. Samples from the Gabal Gerf 750 Ma ophiolite do not show this systematic significant deep ocean U addition and likely reflect seawater alteration of ocean crust under anoxic conditions. The Th-U elemental, and U isotopic compositions of Gabal Gerf are consistent with Fe^{3+}/Fe_T ratios of the samples, that reflect anoxic alteration conditions. Our data argue for deep ocean oxygenation between 750 – 540 Ma, but it is not clear if the ophiolite data reflect a full transition or intermittent events within a largely anoxic deep ocean. Nonetheless, U abundances and Th/U ratios of ophiolites are useful tracers of the oxygenation state of deep ocean water during its alteration of the oceanic crust. The U isotope data, that suggest ^{238}U-^{235}U isotopic fractionation during U uptake into ancient AOC similar to processes in modern AOC, provide important supporting information but are less diagnostic given the relatively small isotopic fractionations and ability of different styles of seafloor alteration to cause fractionations in different senses.

Credit authorship contribution statement

Joel B. Rodney: Data curation, formal analysis, investigation, methodology, validation, visualisation, writing – original draft. **Morten B. Andersen:** Supervision, project administration, funding acquisition, conceptualization, methodology, writing – review and editing. **Daniel Stubbs:** Methodology, writing – review and editing. **C. Johan Lissenberg:** Resources, writing – review and editing. **Omar Gianola:** Resources, writing – review and editing. **Matthias Willbold:** Resources, writing – review and editing. **Tim Elliott:** Supervision, project administration, funding acquisition, conceptualization, writing – review and editing.

Declaration of competing interest

The authors declare that they have no known competing financial interests or personal relationships that could have appeared to influence the work reported in this paper.

Data availability

Data are available through Mendeley data at:
https://data.mendeley.com/datasets/fyk72sg4km/4

Acknowledgments

JBR would like to acknowledge Christopher D. Coath and Carolyn Taylor for the upkeep of the labs. JBR would like to acknowledge Ian Parkinson, Paul Savage, and Lewis Alcott for useful comments. JBR would like to thank Huiming Bao for editorial handling and Laurence Coogan and three anonymous reviews for helpful comments. JBR was supported by a NERC GW4 + Doctoral Training Partnership studentship from the Natural Environmental Research Council [NE/S007504/1]. JBR, MBA, and TE acknowledge funding from a NERC grant [NE/T012595/1 & NE/T012633/1].

Appendix A. Supplementary Material

Supplementary Material related to this article can be found online at:

References

Algeo, T. J., and C. Li, 2020, Redox classification and calibration of redox thresholds in sedimentary systems: Geochimica et Cosmochimica Acta, **287**, 8–26.

Alt, J., 2004, Alteration of the upper oceanic crust: mineralogy, chemistry, and processes: Hydrogeology of the Oceanic Lithosphere, 456–488.

Alt, J. C., and J. Honnorez, 1984, Alteration of the upper oceanic crust, DSDP site 417: mineralogy and chemistry: Contributions to Mineralogy and Petrology, **87**, 149–169.

Alt, J. C., and D. A. H. Teagle, 2003, Hydrothermal alteration of upper oceanic crust formed at a fast-spreading ridge: mineral, chemical, and isotopic evidence from ODP Site 801: Chemical Geology, **201**, 191–211.

Alt, J. C., C. Laverne, R. M. Coggon, D. A. H. Teagle, N. R. Banerjee, S. Morgan, C. E. Smith-Duque, M. Harris, and L. Galli, 2010, Subsurface structure of a submarine hydrothermal system in ocean crust formed at the East Pacific Rise, ODP/IODP Site 1256: Submarine hydrothermal system: Geochemistry, Geophysics, Geosystems, **11**, Q10010.

Andersen, M. B., S. Romaniello, D. Vance, S. H. Little, R. Herdman, and T. W. Lyons, 2014, A modern framework for the interpretation of $^{238}U/^{235}U$ in studies of ancient ocean redox: Earth and Planetary Science Letters, **400**, 184–194.

Andersen, M. B., T. Elliott, H. Freymuth, K. W. W. Sims, Y. Niu, and K. A. Kelley, 2015, The terrestrial uranium isotope cycle: Nature, **517**, 356–359.

Andersen, M. B., J. B. Rodney, H. Freymuth, F. Vils, M. Harris, K. Cooper, D. A. H. Teagle, and T. Elliott, 2024, Time scales and mechanisms of uranium uptake in altered ocean crust; observations from the ∼15 million year-old site 1256 in the eastern equatorial Pacific: Geochimica et Cosmochimica Acta, **382**, 142–159.

Anderson, R. F., M. Q. Fleisher, and A. P. LeHuray, 1989, Concentration, oxidation state, and particulate flux of uranium in the Black Sea: Geochimica et Cosmochimica Acta, **53**, 2215–2224.

Bach, W., B. Peucker-Ehrenbrink, S. R. Hart, and J. S. Blusztajn, 2003, Geochemistry of hydrothermally altered oceanic crust: DSDP/ODP Hole 504B - Implications for seawater-crust exchange budgets and Sr- and Pb-isotopic evolution of the mantle: Hydrothermally altered oceanic crust: Geochemistry, Geophysics, Geosystems, **4**, 8904.

Bacon, M. P., 1978, Radioactive disequilibrium in altered mid-oceanic basalts: Earth and Planetary Science Letters, **39**, 250–254.

Butterfield, N. J., 2007, Macroevolution and Macroecology Through Deep Time: Palaeontology, **50**, 41–55.

Canfield, D. E., 1998, A new model for Proterozoic ocean chemistry: Nature, **396**, 450–453.

Canfield, D. E., 2014, 6.8 - Proterozoic Atmospheric Oxygen, *in* H. D. Holland and K. K. Turekian, eds., Treatise on Geochemistry (Second Edition), Elsevier, 197–216.

Canfield, D. E., S. W. Poulton, and G. M. Narbonne, 2007, Late-Neoproterozoic Deep-Ocean Oxygenation and the Rise of Animal Life: Science, **315**, 92–95.

Canfield, D. E., S. W. Poulton, A. H. Knoll, G. M. Narbonne, G. Ross, T. Goldberg, and H. Strauss, 2008, Ferruginous conditions dominated later neoproterozoic deep-water chemistry: Science (New York, N.Y.), **321**, 949–952.

Chabaux, F., J. Riotte, and O. Dequincey, 2003, U-Th-Ra Fractionation During Weathering and River Transport: Reviews in Mineralogy and Geochemistry, **52**, 533–576.

Chen, B., C. Hu, B. J. W. Mills, T. He, M. B. Andersen, X. Chen, P. Liu, M. Lu, R. J. Newton, S. W. Poulton, G. A. Shields, and M. Zhu, 2022, A short-lived oxidation event during the early Ediacaran and delayed oxygenation of the Proterozoic ocean: Earth and Planetary Science Letters, **577**, 117274.

Cheng, H., R. Lawrence Edwards, C.-C. Shen, V. J. Polyak, Y. Asmerom, J. Woodhead, J. Hellstrom, Y. Wang, X. Kong, C. Spötl, X. Wang, and E. Calvin Alexander, 2013, Improvements in ^{230}Th dating, ^{230}Th and ^{234}U half-life values, and U–Th isotopic measurements by multi-collector inductively coupled plasma mass spectrometry: Earth and Planetary Science Letters, **371–372**, 82–91.

Dahl, T. W., R. A. Boyle, D. E. Canfield, J. N. Connelly, B. C. Gill, T. M. Lenton, and M. Bizzarro, 2014, Uranium isotopes distinguish two geochemically distinct stages during the later Cambrian SPICE event: Earth and Planetary Science Letters, **401**, 313–326.

Dahl, T. W., E. U. Hammarlund, A. D. Anbar, D. P. G. Bond, B. C. Gill, G. W. Gordon, A. H. Knoll, A. T. Nielsen, N. H. Schovsbo, and D. E. Canfield, 2010, Devonian rise in atmospheric oxygen correlated to the radiations of terrestrial plants and large predatory fish: Proceedings of the National Academy of Sciences, **107**, 17911–17915.

Dang, D. H., W. Wang, T. M. Gibson, M. Kunzmann, M. B. Andersen, G. P. Halverson, and R. D. Evans, 2022, Authigenic uranium isotopes of late Proterozoic black shale: Chemical Geology, **588**, 120644.

Dunk, R. M., R. A. Mills, and W. J. Jenkins, 2002, A reevaluation of the oceanic uranium budget for the Holocene: Chemical Geology, **190**, 45–67.

Dunning, G., and T. Krogh, 1985, Geochronology of ophiolites of the Newfoundland Appalachians: Canadian Journal of Earth Sciences, **22**, 1659–1670.

Gale, A., C. A. Dalton, C. H. Langmuir, Y. Su, and J.-G. Schilling, 2013, The mean composition of ocean ridge basalts: Geochemistry, Geophysics, Geosystems, **14**, 489–518.

Gaschnig, R. M., C. T. Reinhard, N. J. Planavsky, X. Wang, D. Asael, and M. G. Jackson, 2021, The impact of primary processes and secondary alteration on the stable isotope composition of ocean island basalts: Chemical Geology, **581**, 120416.

Gianola, O., M. W. Schmidt, O. Jagoutz, J. Rickli, O. Bruguier, and O. Sambuu, 2019, The Crust–Mantle Transition of the Khantaishir Arc Ophiolite (Western Mongolia): Journal of Petrology, **60**, 673–700.

Gillis, K. M., L. A. Coogan, and C. Brant, 2015, The role of sedimentation history and lithology on fluid flow and reactions in off-axis hydrothermal systems: A perspective from the Troodos ophiolite: Chemical Geology, **414**, 84–94.

Hart, S. R., and H. Staudigel, 1982, The control of alkalies and uranium in seawater by ocean crust alteration: Earth and Planetary Science Letters, **58**, 202–212.

Holland, H. D., 1984, The Chemical Evolution of the Atmosphere and Oceans: Princeton Univ. Press, Princeton.

Jian, P., A. Kröner, B. Jahn, B. Windley, Y. Shi, W. Zhang, F. Zhang, L. Miao, D. Tomurhuu, and D. Liu, 2014, Zircon dating of Neoproterozoic and Cambrian ophiolites in West Mongolia and implications for the timing of orogenic processes in the central part of the Central Asian Orogenic Belt: Earth-Science Reviews, **133**.

Kelley, K. A., T. Plank, J. Ludden, and H. Staudigel, 2003, Composition of altered oceanic crust at ODP Sites 801 and 1149: Geochemistry, Geophysics, Geosystems, **4**, 8910.

Kipp, M. A., H. Li, M. J. Ellwood, S. G. John, R. Middag, J. F. Adkins, and F. L. H. Tissot, 2022, 238U, 235U and 234U in seawater and deep-sea corals: A high-precision reappraisal: Geochimica et Cosmochimica Acta, **336**, 231–248.

Klinkhammer, G. P., and M. R. Palmer, 1991, Uranium in the oceans: Where it goes and why: Geochimica et Cosmochimica Acta, **55**, 1799–1806.

Krause, A. J., B. J. W. Mills, A. S. Merdith, T. M. Lenton, and S. W. Poulton, 2022, Extreme variability in atmospheric oxygen levels in the late Precambrian: Science Advances, **8**, eabm8191.

Krause, A. J., B. J. W. Mills, S. Zhang, N. J. Planavsky, T. M. Lenton, and S. W. Poulton, 2018, Stepwise oxygenation of the Paleozoic atmosphere: Nature Communications, **9**, 4081.

Kröner, A., W. Todt, I. M. Hussein, M. Mansour, and A. A. Rashwan, 1992, Dating of late Proterozoic ophiolites in Egypt and the Sudan using the single grain zircon evaporation technique: Precambrian Research, **59**, 15–32.

Langmuir, D., 1978, Uranium solution-mineral equilibria at low temperatures with applications to sedimentary ore deposits: Geochimica et Cosmochimica Acta, **42**, 547–569.

Lenton, T. M., R. A. Boyle, S. W. Poulton, G. A. Shields-Zhou, and N. J. Butterfield, 2014, Co-evolution of eukaryotes and ocean oxygenation in the Neoproterozoic era: Nature Geoscience, **7**, 257–265.

Lissenberg, C. J., J. H. Bédard, and C. R. van Staal, 2004, The structure and geochemistry of the gabbro zone of the Annieopsquotch ophiolite, Newfoundland: implications for lower crustal accretion at spreading ridges: Earth and Planetary Science Letters, **229**, 105–123.

Lissenberg, C. J., C. R. van Staal, J. H. Bédard, and A. Zagorevski, 2005, Geochemical constraints on the origin of the Annieopsquotch ophiolite belt, Newfoundland Appalachians: Geological Society of America Bulletin, **117**, 1413.

Lyons, T. W., C. T. Reinhard, and N. J. Planavsky, 2014, The rise of oxygen in Earth's early ocean and atmosphere: Nature, **506**, 307–315.

Lyons, T. W., C. W. Diamond, N. J. Planavsky, C. T. Reinhard, and C. Li, 2021, Oxygenation, Life, and the Planetary System during Earth's Middle History: An Overview: Astrobiology, **21**, 906–923.

Lyons, T. W., C. J. Tino, G. P. Fournier, R. E. Anderson, W. D. Leavitt, K. O. Konhauser, and E. E. Stüeken, 2024, Co-evolution of early Earth environments and microbial life: Nature Reviews Microbiology, **22**, 572–586.

MacDougall, J. D., R. C. Finkel, J. Carlson, and S. Krishnaswami, 1979, Isotopic evidence for uranium exchange during low-temperature alteration of oceanic basalt: Earth and Planetary Science Letters, **42**, 27–34.

Mills, B. J. W., A. J. Krause, I. Jarvis, and B. D. Cramer, 2023, Evolution of Atmospheric O2 Through the Phanerozoic, Revisited: Annual Review of Earth and Planetary Sciences, **51**, 253–276.

Noordmann, J., S. Weyer, R. B. Georg, S. Jöns, and M. Sharma, 2016, $^{(238)}U/^{(235)}U$ isotope ratios of crustal material, rivers and products of hydrothermal alteration: new insights

on the oceanic U isotope mass balance: Isotopes in Environmental and Health Studies, **52**, 141–163.

Osmond, J. K., and J. B. Cowart, 1976, The theory and uses of natural uranium isotopic variations in hydrology: Atomic Energy Review, **14**, 621–679.

Partin, C. A., A. Bekker, N. J. Planavsky, C. T. Scott, B. C. Gill, C. Li, V. Podkovyrov, A. Maslov, K. O. Konhauser, S. V. Lalonde, G. D. Love, S. W. Poulton, and T. W. Lyons, 2013, Large-scale fluctuations in Precambrian atmospheric and oceanic oxygen levels from the record of U in shales: Earth and Planetary Science Letters, **369–370**, 284–293.

Pavia, F. J., E. H. G. Cooperdock, J. C. de Obeso, K. W. W. Sims, F. L. H. Tissot, and F. Klein, 2023, Uranium isotopes as tracers of serpentinite weathering: Earth and Planetary Science Letters, **623**, 118434.

Planavsky, N. J., C. T. Reinhard, X. Wang, D. Thomson, P. McGoldrick, R. H. Rainbird, T. Johnson, W. W. Fischer, and T. W. Lyons, 2014, Low Mid-Proterozoic atmospheric oxygen levels and the delayed rise of animals: Science, **346**, 635–638.

Planavsky, N. J., P. McGoldrick, C. T. Scott, C. Li, C. T. Reinhard, A. E. Kelly, X. Chu, A. Bekker, G. D. Love, and T. W. Lyons, 2011, Widespread iron-rich conditions in the mid-Proterozoic ocean: Nature, **477**, 448–451.

Regelous, M., K. M. Haase, S. Freund, M. Keith, C. G. Weinzierl, C. Beier, P. A. Brandl, T. Endres, and H. Schmidt, 2014, Formation of the Troodos Ophiolite at a triple junction: Evidence from trace elements in volcanic glass: Chemical Geology, **386**, 66–79.

Richter, S., A. Alonso-Munoz, R. Eykens, U. Jacobsson, H. Kuehn, A. Verbruggen, Y. Aregbe, R. Wellum, and E. Keegan, 2008, The isotopic composition of natural uranium samples - Measurements using the new $n^{(233U)}/n^{(236U)}$ double spike IRMM-3636: International Journal of Mass Spectrometry, **269**, 145–148.

Robbins, L. J., S. V. Lalonde, N. J. Planavsky, C. A. Partin, C. T. Reinhard, B. Kendall, C. Scott, D. S. Hardisty, B. C. Gill, D. S. Alessi, C. L. Dupont, M. A. Saito, S. A. Crowe, S. W. Poulton, A. Bekker, T. W. Lyons, and K. O. Konhauser, 2016, Trace elements at the intersection of marine biological and geochemical evolution: Earth-Science Reviews, **163**, 323–348.

Sahoo, S. K., N. J. Planavsky, G. Jiang, B. Kendall, J. D. Owens, X. Wang, X. Shi, A. D. Anbar, and T. W. Lyons, 2016, Oceanic oxygenation events in the anoxic Ediacaran ocean: Geobiology, **14**, 457–468.

Scott, C., T. W. Lyons, A. Bekker, Y. Shen, S. W. Poulton, X. Chu, and A. D. Anbar, 2008, Tracing the stepwise oxygenation of the Proterozoic ocean: Nature, **452**, 456–459.

Seyedali, M., L. A. Coogan, and K. M. Gillis, 2021, Li-isotope exchange during low-temperature alteration of the upper oceanic crust at DSDP Sites 417 and 418: Geochimica et Cosmochimica Acta, **294**, 160–173.

Sperling, E. A., C. J. Wolock, A. S. Morgan, B. C. Gill, M. Kunzmann, G. P. Halverson, F. A. Macdonald, A. H. Knoll, and D. T. Johnston, 2015, Statistical analysis of iron geochemical data suggests limited late Proterozoic oxygenation: Nature, **523**, 451–454.

Stockey, R. G., D. B. Cole, U. C. Farrell, H. Agić, T. H. Boag, J. J. Brocks, D. E. Canfield, M. Cheng, P. W. Crockford, H. Cui, T. W. Dahl, L. Del Mouro, K. Dewing, S. Q. Dornbos, J. F. Emmings, R. R. Gaines, T. M. Gibson, B. C. Gill, G. J. Gilleaudeau, K. Goldberg, R. Guilbaud, G. Halverson, E. U. Hammarlund, K. Hantsoo, M. A. Henderson, C. M. Henderson, M. S. W. Hodgskiss, A. J. M. Jarrett, D. T. Johnston, P. Kabanov, J. Kimmig, A. H. Knoll, M. Kunzmann, M. A. LeRoy, C. Li, D. K. Loydell, F. A. Macdonald, J. M. Magnall, N. T. Mills, L. M. Och, B. O'Connell, A. Pagès, S. E. Peters, S. M. Porter, S. W. Poulton, S. R. Ritzer, A. D. Rooney, S. Schoepfer, E. F. Smith, J. V. Strauss, G. J. Uhlein, T. White, R. A. Wood, C. R. Woltz, I. Yurchenko, N. J. Planavsky, and E. A. Sperling, 2024, Sustained increases in atmospheric oxygen and marine productivity in the Neoproterozoic and Palaeozoic eras: Nature Geoscience, **17**, 667–674.

Stolper, D. A., and C. B. Keller, 2018, A record of deep-ocean dissolved O_2 from the oxidation state of iron in submarine basalts: Nature, **553**, 323–327.

Stolper, D. A., X. Pu, M. K. Lloyd, N. I. Christensen, C. E. Bucholz, and R. A. Lange, 2022, Constraints on Early Paleozoic Deep-Ocean Oxygen Concentrations From the Iron Geochemistry of the Bay of Islands Ophiolite: Geochemistry, Geophysics, Geosystems, **23**, e2021GC010196.

Sylwester, E. R., E. A. Hudson, and P. G. Allen, 2000, The structure of uranium (VI) sorption complexes on silica, alumina, and montmorillonite: Geochimica et Cosmochimica Acta, **64**, 2431–2438.

Thurber, D. L., 1962, Anomalous U 234 U 238 in nature: Journal of Geophysical Research, **67**, 11, 4518-4520.

Tostevin, R., and B. J. W. Mills, 2020, Reconciling proxy records and models of Earth's oxygenation during the Neoproterozoic and Palaeozoic: Interface Focus, **10**, 20190137.

Wei, G.-Y., N. J. Planavsky, T. He, F. Zhang, R. G. Stockey, D. B. Cole, Y.-B. Lin, and H.-F. Ling, 2021, Global marine redox evolution from the late Neoproterozoic to the early

Paleozoic constrained by the integration of Mo and U isotope records: Earth-Science Reviews, **214**, 103506.

Zimmer, M., A. Kröner, K. P. Jochum, T. Reischmann, and W. Todt, 1995, The Gabal Gerf complex: A precambrian N-MORB ophiolite in the Nubian Shield, NE Africa: Chemical Geology, **123**, 29–51.

Assessing the timing of deep ocean oxygenation from uranium elemental and isotopic compositions of ophiolites

Joel B. Rodney[a*], Morten B. Andersen[b], Daniel Stubbs[a, c], C. Johan Lissenberg[b], Omar Gianola[d], Matthias Willbold[e], Tim Elliott[a]

[a]Bristol Isotope Group, School of Earth Sciences, University of Bristol, Wills Memorial Building, Queen's Road, Bristol, BS8 1RJ, UK

[b]School of Earth & Environmental Sciences, Cardiff University, Park Place, Cardiff, CF10 3AT, UK

[c]National Nuclear Laboratory, Central Laboratory, Sellafield, Cumbria, UK, CA20 1PG

[d]Department of Geosciences, University of Padova, Via G. Gradenigo 6, 35131 Padova, Italy

[e]Georg-August-Universität Göttingen, Geowissenschaftliches Zentrum Göttingen, Abt. Geochemie und Isotopengeologie, Goldschmidtstr. 1, 37077 Göttingen, Germany

*Corresponding author

Email addresses: joel.rodney@bristol.ac.uk (J.B. Rodney), andersenm1@cardiff.ac.uk (M.B. Andersen), dstubbs95@icloud.com (D. Stubbs), lissenbergcj@cardiff.ac.uk (C. J. Lissenberg), omar.gianola.res@gmail.com (O. Gianola), matthias.willbold@uni-goettingen.de (M. Willbold), tim.elliott@bristol.ac.uk (T. Elliott).

Supplementary Information

Section 1: Relative Thorium to Niobium and tectonic setting differences of mantle basalts and ophiolite samples & Alteration mineralogy

Section 2: Full detailed method description for U isotopic analysis

Section 3: Ophiolite data and data tables

Section 4: Recent U addition from a groundwater source modelling

Section 5: Iron systematics

Section 1:

Relative Thorium to Niobium and tectonic setting differences of mantle basalts and ophiolite samples

Relative Th to Nb concentrations can differentiate tectonic settings of ophiolite formation, with suprasubduction zone settings showing elevated incompatible element signatures similar to arc lavas, e.g., elevated Th relative to Nb (Dilek and Furnes, 2011) (Fig. S1a). Gabal Gerf samples mostly overlap with mid-ocean ridge basalts (MORB) from mid-ocean ridge spreading centres (Zimmer et al., 1995). Khantaishir samples overlap with volcanic arc samples, indicating an enriched source in a suprasubduction zone setting (Gianola et al., 2019). Annieopsquotch samples fall in-between the two and can be identified as MORB with a slight suprasubduction zone signature, forming in a back-arc setting (Lissenberg et al., 2005) (Fig. S1a). The variability in tectonic setting is not significant for this study, as the U signatures being compared are imparted during secondary alteration, likely overprinting any primary signature differences. One potential issue relates to Th/U ratios and how much these differ between fresh magmas in different tectonic settings. A key indicator of U enrichment during alteration is a lowering of Th/U. If basalts from different tectonic settings have different starting Th/U ratios, this can make identification of alteration using Th/U ratios challenging. However, no systematic difference in the Th/U ratio of basalt formed in spreading centres and back arcs is seen, and only a small difference with volcanic arcs that extend to lower Th/U, presumably due to some U addition from slab dehydration (Fig. S1b). Even then, volcanic arc lavas have only slightly lower average Th/U (~ 2.3, Fig. S1b), which is not as low as the majority of samples that show high U enrichments in modern altered oceanic crust (AOC) (Fig. S1b), with for example the average Th/U of extrusive samples from ODP 1256D being ~ 1.9 (Andersen et al., 2024). Therefore, given this and the reasons given in the main text, we see no reason to treat ophiolite samples from different tectonic settings differently, as the main indicators we are looking for from seawater alteration overprint any primary differences from different tectonic settings.

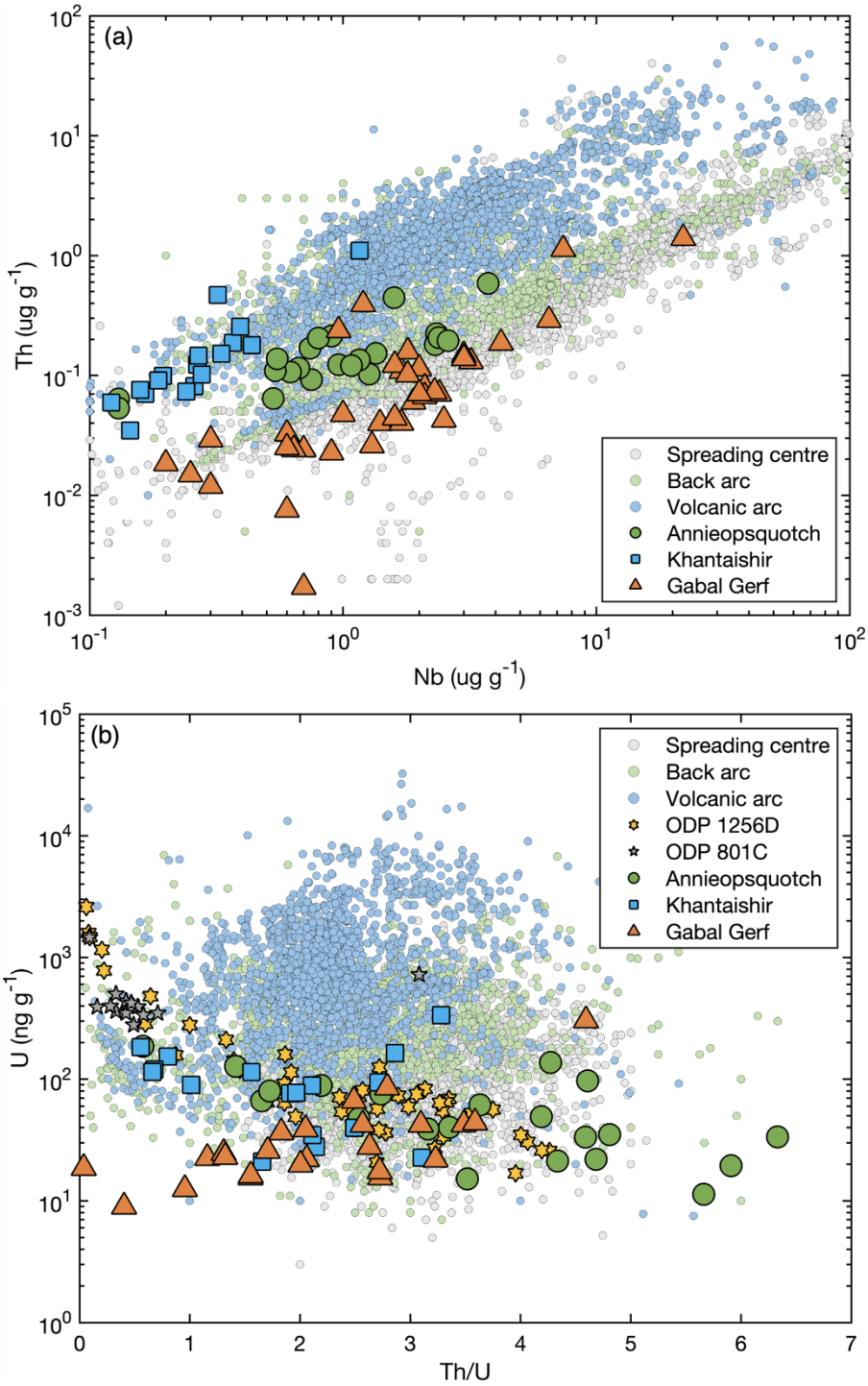

Fig. S1. (a) Th vs. Nb concentration and (b) U concentration vs. Th/U ratio for ophiolite samples and analyses of whole rock and glass samples from spreading centres, back arcs, and volcanic arcs, and ODP 1256D and 801C. Literature data for back arc and volcanic arc samples downloaded from PetDB on 23/09/2021 using data for whole rock and glass samples, data for spreading centres is from the N-MORB dataset from Gale et al. (2013). Data for ODP 1256D and 801C are from Andersen et al. (2024) and Andersen et al. (2015) respectively. Measurements for ophiolite samples are from Element2 ICP-MS measurements and isotope dilution measurements (U), and Nb data from - Annieopsquotch - Lissenberg et al. (2005), Khantaishir - Gianola et al. (2019), and Gabal Gerf - Zimmer et al. (1995).

Alteration mineralogy

The main host minerals and sites for U in AOC are poorly constrained, but current perspectives suggest that U uptake under oxic conditions in the shallow crust is associated with phases such as celadonite and Fe-oxyhydroxides, while under more reducing conditions in deeper portions of the crust uptake is associated with carbonates and in redox haloes (e.g., Staudigel et al., 1996; Bach et al., 2003; Kelley et al., 2005; Andersen et al., 2015, 2024).

Representative samples from the Annieopsquotch and Khantaishir ophiolites have textures and mineralogy that are indicative of seafloor alteration of extrusive basalt lavas, sheeted dykes, and gabbro. Sample VL01J200a, a pillow basalt with a porphyritic texture that shows U enrichment, has pervasive alteration that overprints some of the primary igneous minerals and textures (Fig. S2a-b). There are brown rims of saponite overprinted with Fe-oxyhydroxides around vesicles filled with turquoise green celadonite. There are some larger phenocrysts of clinopyroxene altered to dusty clinopyroxene with corroded rims and chlorite. The groundmass is made of thin needle laths of plagioclase altered to sericite and saussurite and glass that is altered to palagonite, fine grain secondary phyllosilicate minerals such as micas, smectites and chlorite, and overprinted with dark brown Fe-oxyhydroxides. These alteration minerals are common in upper sections of AOC (e.g., Alt et al., 2010 their figure 2), altered under oxidising conditions, also reflected in the low $\delta^{238}U$ composition (−0.565 ±0.032 ‰, 2SE) and a high U concentration (Table S3). This pattern of alteration is also evident in other samples from the extrusive section of Annieopsquotch such as in sample VL01J205b, that also shows U enrichment, with rounded vesicles filled with celadonite and veins with fibrous needle like celadonite and brown saponite that is also overprinted with dark brown Fe-oxyhydroxides, all indicative of seafloor hydrothermal alteration under oxidising conditions (Fig. S2c-d). Some of the extrusive samples (e.g., VL01J202) are lava breccias and while this sample does not show significant U enrichment it does show similar patterns of alteration to other enriched Annieopsquotch samples, with large phenocrysts (altered plagioclase and pyroxene, altered to phases such as sericite, saussurite, dusty clinopyroxene and chlorite) in an altered fine-grained cement of palagonite, saponite, and Fe-oxyhydroxides (Fig. S2e). Sample VL01J200b, a basaltic dyke within the Annieopsquotch ophiolite extrusive section, has only 6 ng g^{-1} U, reflecting either no U addition or U loss. Unlike the basalt that it crosscuts (VL01J200a, see above), it retains a primary igneous ophitic texture, with laths of plagioclase encased by clinopyroxene, with some plagioclase altered to fine grained sericite (Fig. S2f). The sheeted

dyke samples from Annieopsquotch also show alteration mineralogy indicative of seafloor alteration but are less altered than the extrusive samples with much of the coarse grained primary igneous minerals and textures preserved. Sample VL01J189 has large elongate phenocrysts of plagioclase slightly altered to sericite and phenocrysts of clinopyroxene that are partly corroded and altered to dusty clinopyroxene (Fig. S2g).

Samples from the Khantaishir ophiolite also show alteration mineralogy and textures indicative of seafloor alteration. Sample KTB4, a basaltic andesite from the sill and dyke complex, has a fine-grained groundmass in which some primary clinopyroxene and plagioclase are preserved, while larger phenocrysts are replaced by phases such as calcite (Fig. S2h). This sample shows U enrichment and a U isotopic composition that is higher than some other extrusive samples and is similar to or just higher than modern MORB (−0.201 ±0.016 ‰, 2SE) (Fig. 2, Table S3), potentially reflecting partial reduction and U uptake processes, with reducing conditions of alteration more dominate in lower crustal sections (e.g., Alt et al., 2010 their figure 2). A sample from a similar location in the sill and dyke complex, KT-11-110, with a lower level of U enrichment, has some secondary calcite that is also associated with epidote around its rim and alteration to secondary minerals such as celadonite and phyllosilicate minerals such as micas, smectites and chlorite (Fig. S2i). These patterns of alteration reflect alteration occurring in deeper sections of crust under higher temperatures, such as seafloor greenschist alteration conditions, and potentially reducing conditions (e.g., Alt et al., 2010 their figure 2). This sample however has a $\delta^{238}U$ composition (−0.302 ±0.017 ‰, 2SE) similar to unaltered MORB in keeping with smaller amounts of U uptake and limited isotope fractionation, or quantitative U uptake. Extrusive section basalts from Khantaishir also show signs of seafloor alteration, with sample KT-11-70, that shows U enrichment, preserving an ophitic texture with laths of plagioclase altered to sericite and phenocrysts of clinopyroxene, in a heavily altered glassy groundmass that is altered to palagonite, brown saponite, brown Fe-oxyhydroxides and green celadonite (Fig. S2j). Samples from Khantaishir that do not show a significant U enrichment also show evidence of primary igneous textures and seafloor alteration. Sample KT-12-56, a gabbro, preserves large euhedral-subhedral crystals of clinopyroxene and plagioclase altered to sericite (Fig. S2k). Sample KTU-4, a sill and dyke complex sample, shows alteration mineralogy indicative of lower crustal sections altered during seafloor alteration with large radial crystals of prehnite (Fig. S2l) (e.g., Alt et al., 2010 their figure 2). Lastly sample KT-11-85, an extrusive basalt sample, preserves a pilotassitic volcanic texture with microlites of plagioclase feldspar aligned sub-parallel in a heavily altered glassy groundmass (Fig. S2m).

These observations reflect the heterogeneous nature of U addition to the oceanic crust during alteration, indicating similar alteration processes between Annieopsquotch, Khantaishir and modern AOC (no thin sections were available for Gabel Gerf). Several observations support an ocean floor origin of the alteration assemblages. First, samples show heterogeneous alteration and preserve domains that have not been overprinted by metamorphism and have primary igneous textures and assemblages. Second, the alteration mineralogy records static conditions, inconsistent with a regional metamorphic overprint. Third, the observed alteration assemblages are similar to seafloor alteration mineralogy of modern AOC and show differences between upper and lower sections of crust. Samples from the extrusive upper sections of oceanic crust preserved in the ophiolites record, dominantly, alteration mineralogy indicative of oxidising conditions with minerals such as celadonite and Fe-oxyhydroxides prevalent. While samples from lower sections of crust such in the sheeted dykes and sill and dyke complexes preserve alteration mineralogy reflecting more reducing and higher temperature conditions, with secondary minerals such as calcite, epidote and prehnite more common. These observations, combined with the descriptions of the ophiolites given in section 2 of the main text, indicate that the alteration mineralogy and geochemistry of the ophiolite samples reflect seafloor alteration of oceanic crust rather than alteration of ophiolite samples syn- or post-obduction. Therefore, we interpret these samples as reflecting seafloor alteration of *in-situ* oceanic crust.

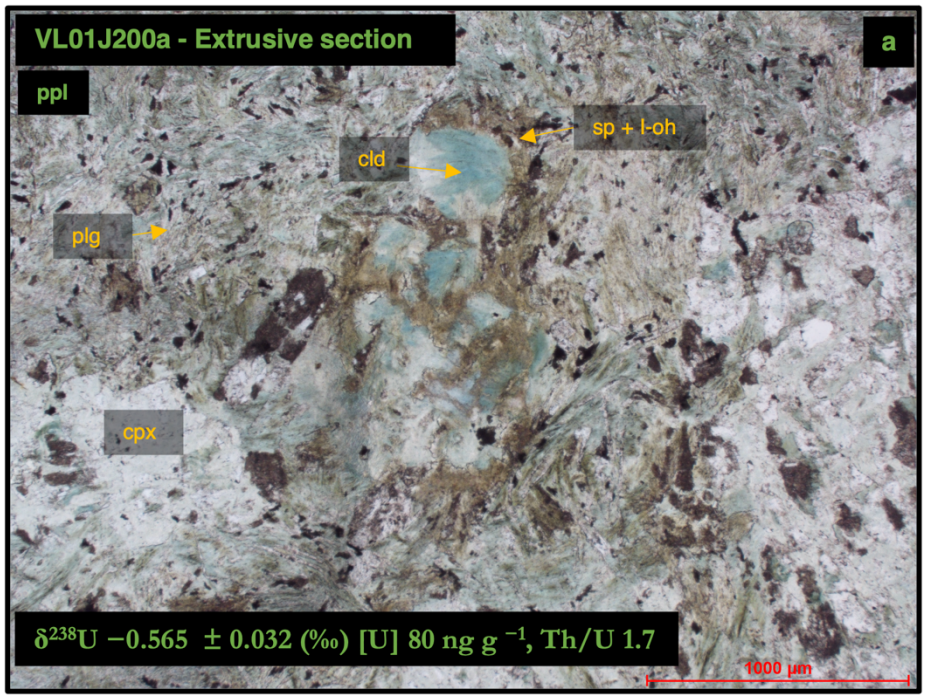
VL01J200a - Extrusive section
a
ppl
sp + l-oh
cld
plg
cpx
δ238U −0.565 ± 0.032 (‰) [U] 80 ng g −1, Th/U 1.7
1000 µm

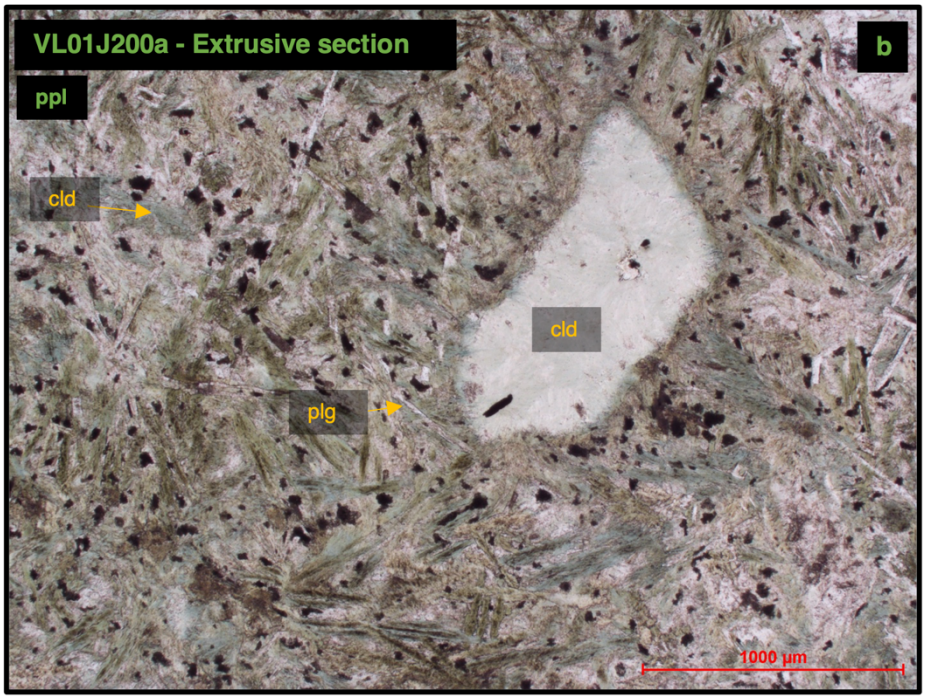
VL01J200a - Extrusive section
b
ppl
cld
cld
plg
1000 µm

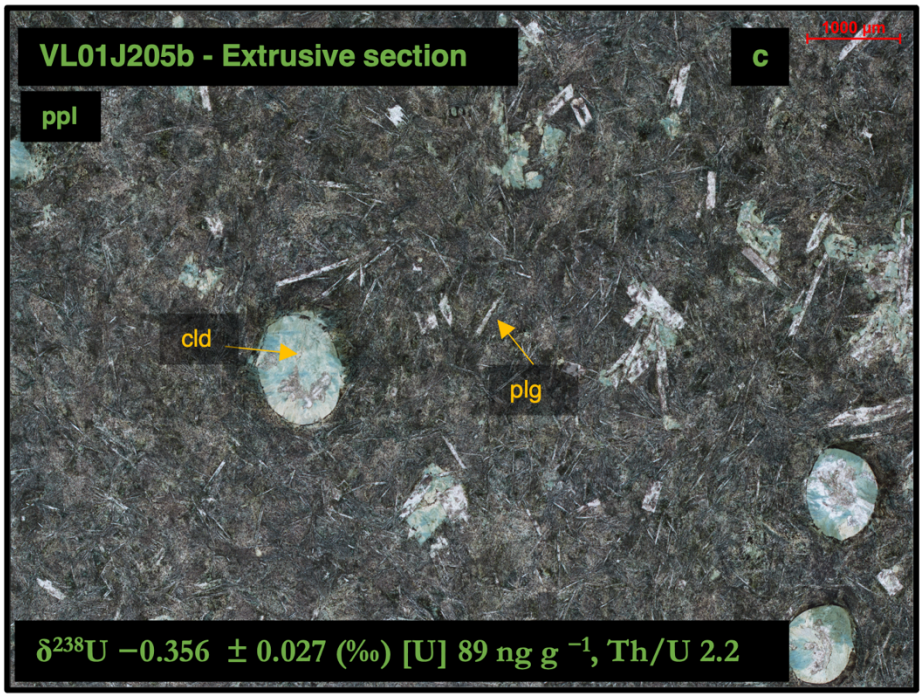
VL01J205b - Extrusive section
c
1000 µm
ppl
cld
plg
δ238U −0.356 ± 0.027 (‰) [U] 89 ng g −1, Th/U 2.2

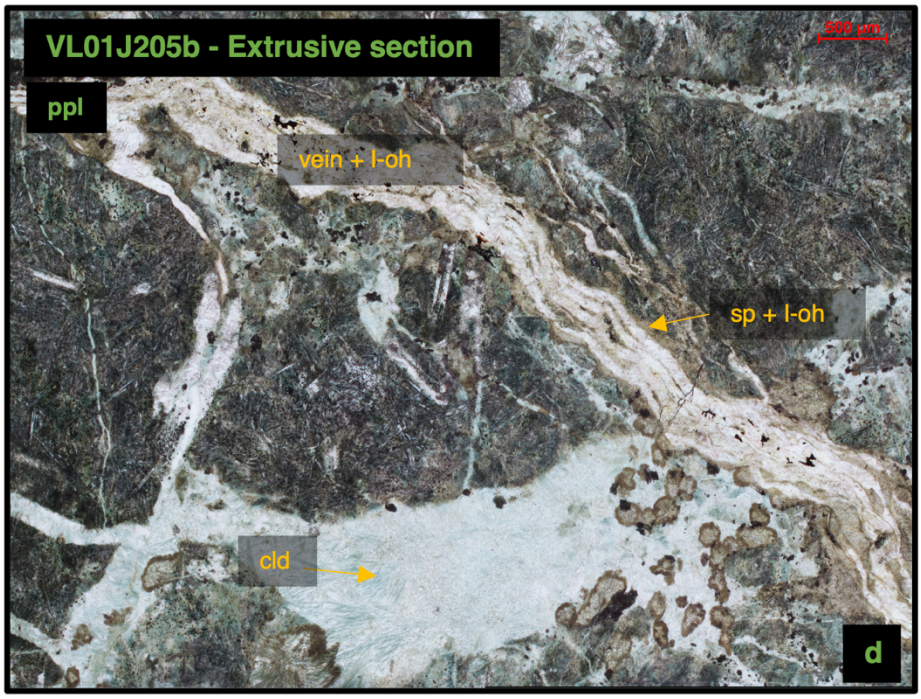
VL01J205b - Extrusive section
500 µm
ppl
vein + l-oh
sp + l-oh
cld
d

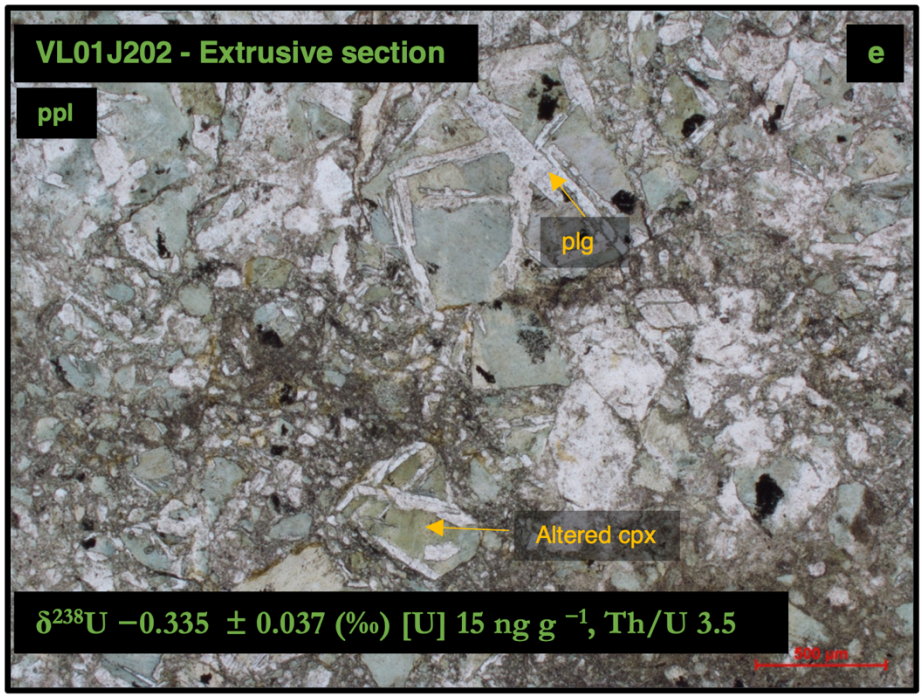
VL01J202 - Extrusive section
e
ppl
plg
Altered cpx
δ238U −0.335 ± 0.037 (‰) [U] 15 ng g −1, Th/U 3.5
500 µm

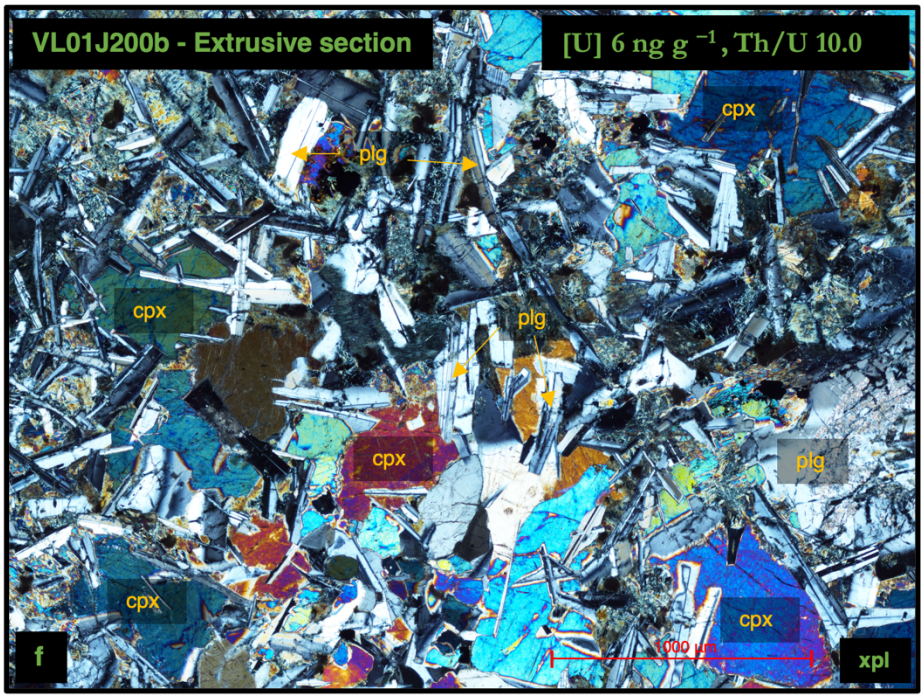
VL01J200b - Extrusive section
[U] 6 ng g −1, Th/U 10.0
cpx
plg
cpx
plg
cpx
plg
cpx
cpx
f
1000 µm
xpl

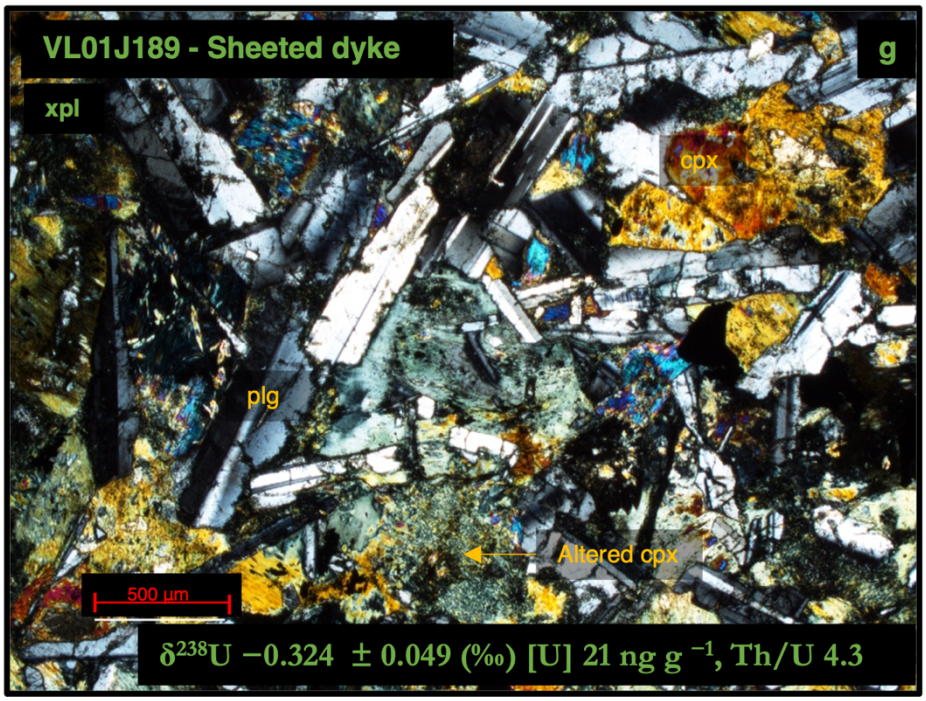
VL01J189 - Sheeted dyke
g
xpl
cpx
plg
Altered cpx
500 µm
δ238U −0.324 ± 0.049 (‰) [U] 21 ng g −1, Th/U 4.3

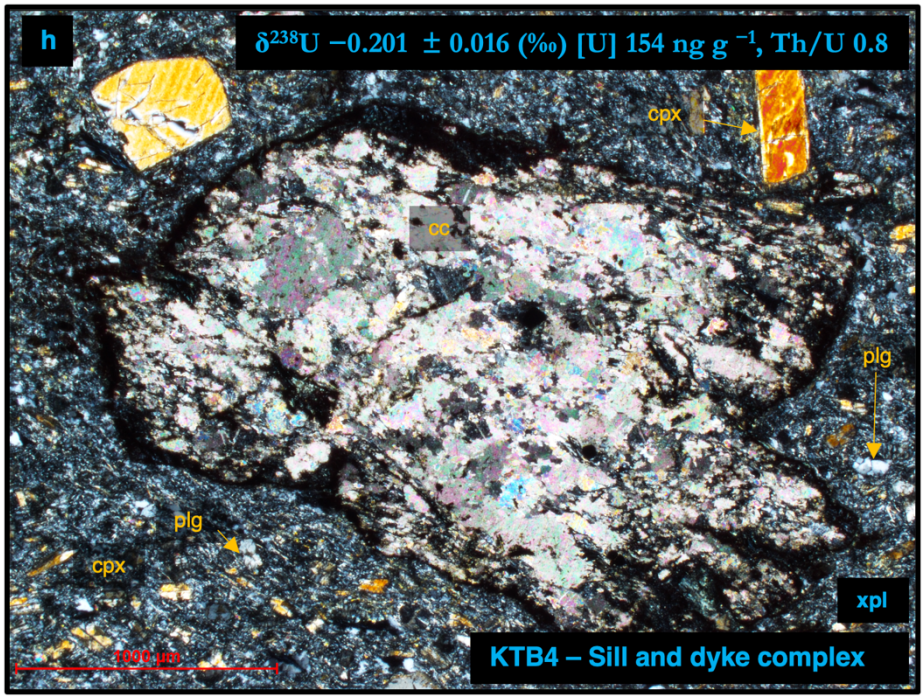
h
δ238U −0.201 ± 0.016 (‰) [U] 154 ng g −1, Th/U 0.8
cpx
cc
plg
plg
cpx
xpl
1000 µm
KTB4 – Sill and dyke complex

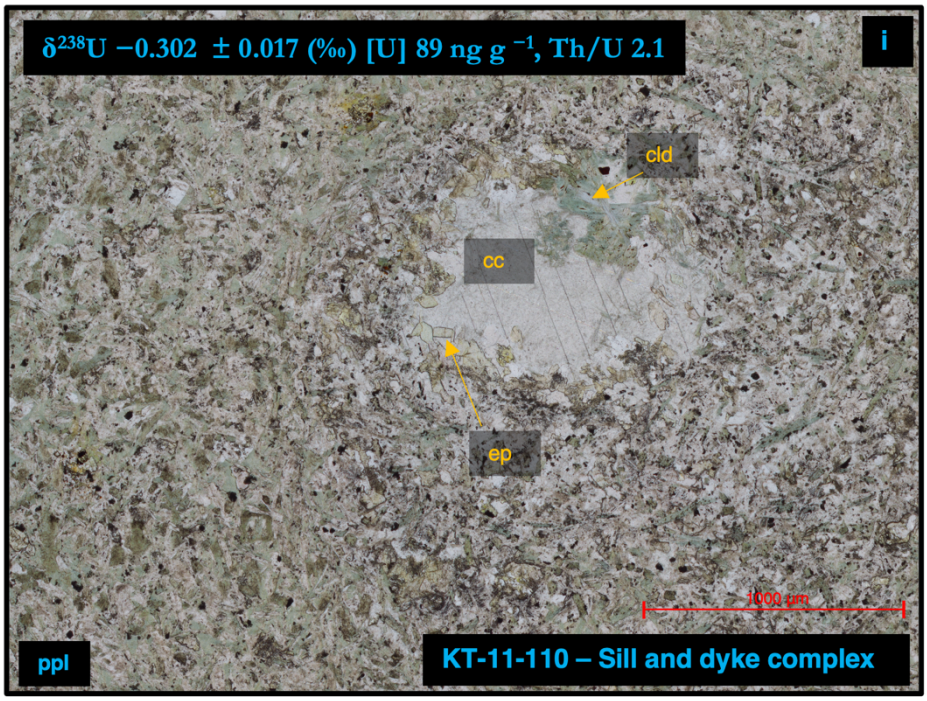
δ238U −0.302 ± 0.017 (‰) [U] 89 ng g −1, Th/U 2.1
i
cld
cc
ep
1000 µm
ppl
KT-11-110 – Sill and dyke complex

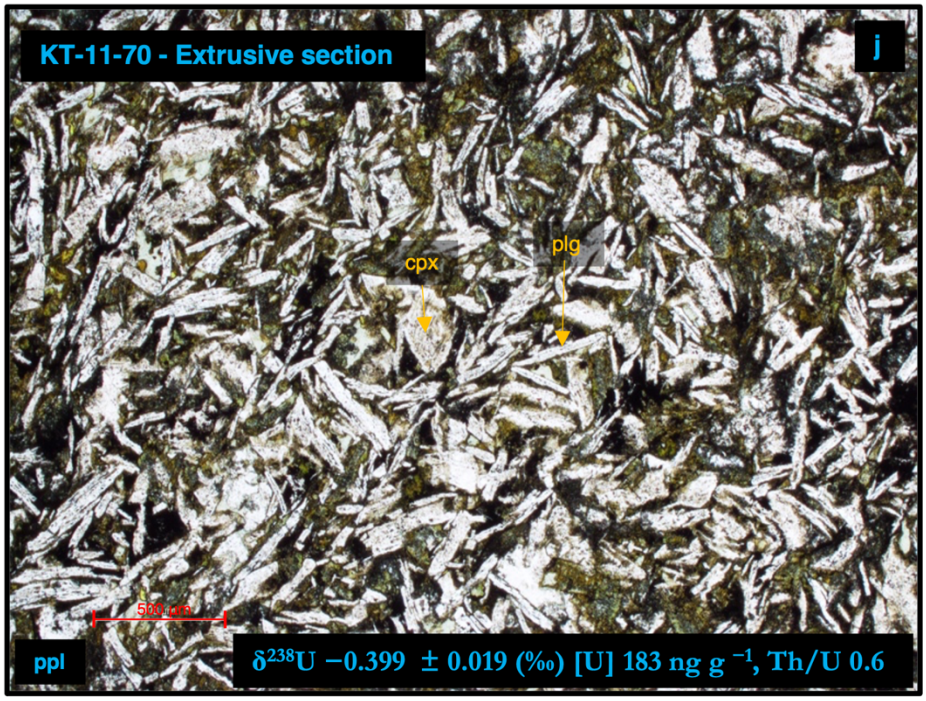
KT-11-70 - Extrusive section
j
cpx
plg
500 µm
ppl
δ238U −0.399 ± 0.019 (‰) [U] 183 ng g −1, Th/U 0.6

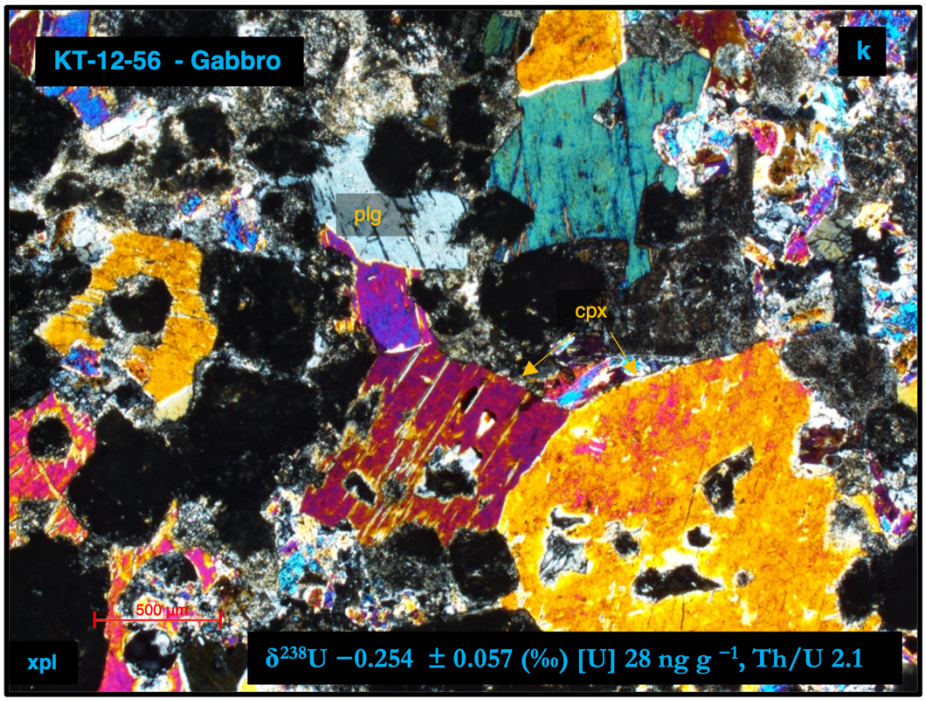
KT-12-56 - Gabbro
k
plg
cpx
500 µm
xpl
δ238U −0.254 ± 0.057 (‰) [U] 28 ng g −1, Th/U 2.1

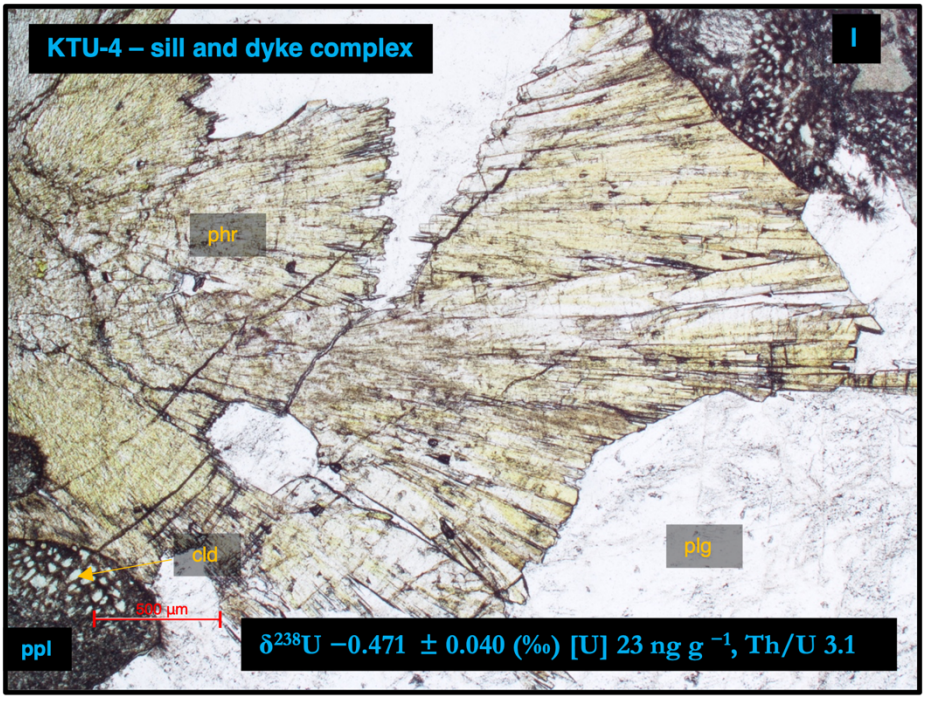
KTU-4 – sill and dyke complex
l
phr
cld
plg
500 µm
ppl
δ238U −0.471 ± 0.040 (‰) [U] 23 ng g −1, Th/U 3.1

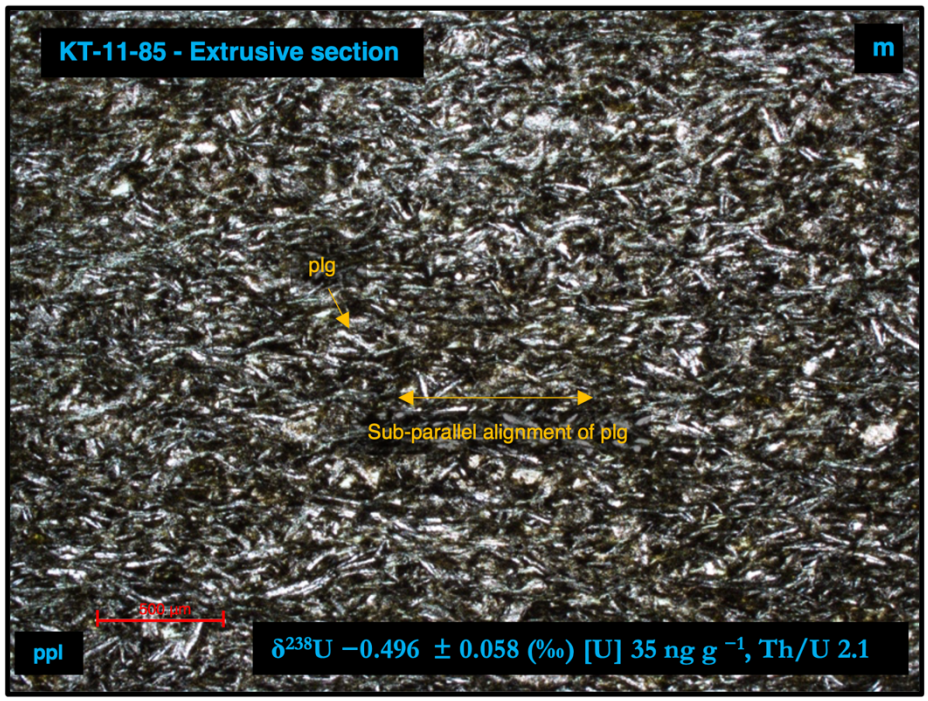

Fig. S2. Photomicrographs of ophiolite samples under plane polarised light (ppl) and cross polarised light (xpl). Scales are 1000 or 500 µm and are shown by red lines. Mineral abbreviations are, plg – Plagioclase feldspar, cpx – Clinopyroxene, cc – Calcite, cld – Celadonite, sp – Saponite, I-oh – Fe-oxyhydroxide, ep – Epidote, phr - Phrenite.

Section 2:

Full detailed method description for U isotopic analysis

Rock powders and associated major and trace element data were obtained for ophiolite samples, with detailed methods referenced to Zimmer et al. (1995), Lissenberg et al. (2005) and Gianola et al. (2019). For the U isotopic measurements, sample preparation and analysis largely followed Andersen et al. (2015) with some modification. Uranium isotope analysis was conducted in the University of Bristol isotope geochemistry laboratories. Approximately 0.5 − 3 g (variable to obtain a given U amount for measurement) of sample powder was digested in pre-cleaned Teflon PFA beakers. one gramme of sample powder was digested in ~ 24 ml of acid (or appropriately scaled volume for different mass samples) using a mixture of 5:1 15.6 M HNO_3 and Romil UpA 28.1 M HF and placed on a tabletop hotplate at 120 °C for at least 48 hours. Samples were then evaporated to dryness and re-dissolved twice in 6 M HCl to remove fluoride precipitates and achieve full sample dissolution. When more than 1 g of sample was required due to low U concentrations, multiple PFA beakers were used to achieve dissolution of separate splits of samples, before partial evaporation and combination into one beaker. For samples that contained large amounts of refractory minerals such as spinel, they were centrifuged, and the supernatant decanted off solid residues. Solid residues were placed in PARR bombs with a mixture of Aqua regia + trace HF at 200 °C for 168 hours. Once full dissolution was achieved samples were recombined and prepared for ion-exchange columns. The double spike tracer, IRMM3636 ^{236}U – ^{233}U, 50:50 (Richter et al., 2008), was added to samples prior to dissolution in most instances, except where multiple aliquots were digested separately and later combined, in this case, the spike was added after recombination of the sample. The double spike was added to samples according to their U concentrations aiming for a $^{236}U/^{235}U$ ratio of 5. For measurement of Th and U concentrations (non-isotope dilution), small amounts of samples (~ 50 mg) were dissolved and measured on an Element2 at the University of Bristol following Andersen et al. (2014).

Samples were loaded in 40 ml of 1.5 M HNO_3 onto 1 ml of TRU resin (100 – 150 mesh) in commercially available Bio-Rad Poly-Prep columns. Matrix was eluted in 30 ml of 1.5 M HNO_3, before U was collected in 11 ml of 0.3 M HF – 0.1 M HCl. Where over 1 g of sample was dissolved the sample was split over multiple columns, with a maximum of 1 g of digested sample being processed using a single column. When samples were divided, the collected aliquots were re-combined post-chemistry. Samples were dried and fluxed in a 1 ml 50:50 15.6

M HNO_3: 30 % Romil SpA H_2O_2 mixture to eliminate any organic material that may have leached off resin into samples. Samples were loaded in 5 ml 3 M HNO_3 onto 0.5 ml of UTEVA resin (100 – 150 mesh), for Th and U separation, with 10 ml of 3 M HNO_3 washed through to elute any residual matrix, before washing through 15 ml of 5 M HCl to elute Th, before collection of U in 6 ml of 0.3 M HF – 0.1 M HCl. Again, any potential organic material was eliminated from samples. Final U collections were then dried and re-dissolved in a requisite amount of 0.2 M HCl (aiming for U concentration of 50 – 300 ng g^{-1}) for isotopic analysis. This procedure achieved efficient removal of Th and Th/U ratios during isotopic analysis were typically <0.005. For samples VL01J188, VL01J191, VL01J 195, VL01J201, and VL01J205b a prior UTEVA chemistry method using 3 M HCl (Andersen et al., 2015) was used for Th separation, this resulted in less efficient Th removal and Th/U ratios ~ 0.1 in measured sample aliquots. A correction for the high mass plus hydride tailing of $^{232}Th^{1}H^{+}$ on the mass 233 and 234 ion beams was applied in these cases.

Uranium isotope compositions were measured on a ThermoFinnigan Neptune MC-ICP-MS (serial no. 1002) at the Bristol Isotope group in low mass resolution (M/ΔM ~ 2000, 5 to 95 % peak height definition), using the setup detailed in Andersen et al. (2015). Samples were introduced to the plasma using a ~ 40 µl min^{-1} micro-concentric PFA nebuliser connected to a Cetac Aridus (1st generation) desolvating system. A standard sample cone plus X-skimmer cone set up was used, with a jet sample cone plus X-skimmer cone method also used for low U concentration samples, which gives enhanced sensitivity allowing for improved precision, results obtained via both set ups are indistinguishable (Andersen et al., 2015). Masses 232 (^{232}Th), 233 (^{233}U), 234 (^{234}U), 236 (^{236}U), and 238 (^{238}U) were collected in faraday cups, with most cups connected to feedback amplifiers with 10^{11} Ω resistors, apart from 234 which was connected to a 10^{12} or 10^{13} Ω resistor (after they became commercially available) and 238 which was connected to a 10^{10} Ω resistor. Each sample was preceded and followed by a measurement of the double-spiked (with a double spike proportion similar to samples) standard CRM-145. Individual measurements consisted of 80 cycles each, with 4.194 s integrations, samples were measured at varying concentrations, generally between 50 − 300 ng g^{-1}, correlating to U consumption between ~ 15 − 80 ng per measurement. Procedural blanks were <30 pg U, an insignificant amount compared to amount of U consumed per measurement. Ion beam intensities were corrected for low mass tailings of ion beams and high mass plus hydride tailings of ion beams following Andersen et al. (2015).

The measured double spike isotope ratio of $^{233}U/^{236}U$ was used with the exponential mass fractionation law to correct for mass fractionation of isotope ratios in samples and bracketing standards (Richter et al., 2008). Ratios were also corrected for the minute ^{238}U, ^{235}U and ^{234}U contributions from the IRM-3636 double spike (Condon et al., 2010; Hiess et al., 2012). Uranium isotope ratios for $^{238}U/^{235}U$ and $^{234}U/^{238}U$ are reported in δ notation with $\delta^{238}U = [(^{238}U/^{235}U_{Sample} / {}^{238}U/^{235}U_{CRM\text{-}145}) - 1]$ and $\delta^{234}U = [(^{234}U/^{238}U_{Sample} / (^{234}U/^{238}U_{CRM\text{-}145}/ (1-0.0386)) - 1]$. By normalising sample measurements to the average of bracketing CRM-145 analyses, this removes second order non-exponential mass bias effects from the analyses. Note that $\delta^{234}U$ values are reported relative to secular equilibrium, where the CRM-145 standard has a $\delta^{234}U$ of −38.6 ‰ relative to secular equilibrium (Cheng et al., 2013).

Long term external reproducibility at various measured U intensities has been estimated using aliquots of the well characterised reference material BHVO-2 measured during different analytical sessions. The external reproducibility of $\delta^{238}U$ and $\delta^{234}U$ for BHVO-2 at various intensities (e.g., ^{238}U = 200 − 1000 pA) ranges from ±0.09 − 0.03 ‰, 2SD, and ±4 − 0.9 ‰, 2SD, respectively. The external reproducibility of unknown samples has been determined from the long-term external reproducibility of BHVO-2 measured at various intensities. As samples were measured at varying intensities (~ ^{238}U = 200 − 1000 pA) depending on the U concentration, BHVO-2 was also ran at varying intensities. Repeat measurements of BHVO-2 were then used to estimate the uncertainty of measurements at a given intensity using the 2SD of BHVO-2 measurements in ranges of intensities. A power law was fit to the data for $\delta^{238}U$ and $\delta^{234}U$ at the different intensities and used to approximate errors for unknown samples. This relationship was then used for samples of a given intensity, from which an approximate 2SD could be calculated and an external 2SE calculated based on the number of repeats (Fig. S2).

Uranium isotopic measurements of international reference materials analysed (BHVO-2, BCR-2, BIR, uraninite, CZ1) agree well with values reported by other studies (Table S1). We also report data for a set of in-house reference materials (LP45d, GUG11, and IT3a) that agree well with previous data, and report data on international reference material W-2A ($\delta^{238}U$ −0.289 ‰ ±0.04, 2SD, and $\delta^{234}U$ 2.1 ‰ ±1.4, 2SD, N = 35), such that it can be used for comparison in further studies. Full list of reference material data is provided in table S1, as well as Element2 ICP-MS reference material measurements in table S2.

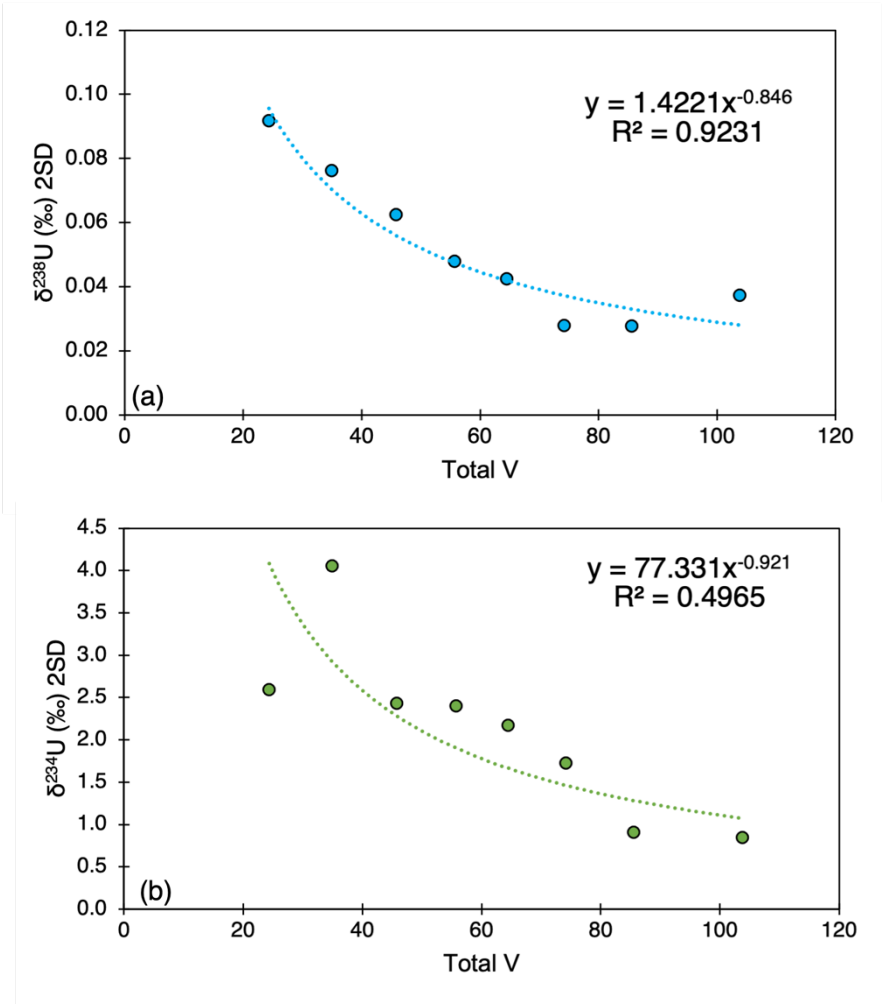

Fig. S3. Error curves for BHVO-2 constructed using the external 2SD of repeat measurements of BHVO-2 at various intensity brackets, 20 − 30 V, 30 − 40 V, 40 − 50 V, 50 − 60 V, 70 − 80 V and >80 V. A power law relationship is fit through the external 2SD. The relationship defined by the power law is then applied to approximate errors for unknown samples. (a) Error curve for $\delta^{238}U$ measurements, (b) Error curve for $\delta^{234}U$ measurements.

Sample	$\delta^{238}U$ (‰)	2SD	$\delta^{234}U$ (‰)	2SD	U (ng g^{-1})$^{+}$	N.M	N.S
BHVO-2	−0.306	0.04	−0.1	1.8	419	145	25
	−0.314	*0.02*	*0.9*	*2.4*	*386*	*16*	*8*
BCR-2	−0.255	0.04	0.6	1.4	1687	27	4
	−0.297	*0.02*	*1.1*	*1.0*	*1671*	*1*	*1*
BIR	−0.277	0.19	−5.1	8.6	8	6	3
	−0.285	*0.02*	*−0.6*	*1.0*	*8*	*1*	*1*
CZ1	−0.048	0.04	−0.2	1.8	7995	30	3
	−0.053	*0.03*	*0.1*	*2.7*		*15*	*2*
GUG11	−0.460	0.05	0.3	2.0	185	10	2
	−0.419	*0.03*	*−0.4*	*2.0*	*143*	*1*	*1*
IT3a	−0.289	0.06	0.1	2.6	70	26	10
	−0.296	*0.02*	*−0.3*	*1.7*	*62*	*3*	*1*
LP45d	−0.319	0.05	−0.2	2.0	2356	83	3
	−0.300	*0.02*	*−0.3*	*4.5*	*2119*	*5*	*2*
Uraninite	−0.548	0.05	−1.5	2.1	11985	51	3
W-2A	−0.291	0.04	2.0	1.4	497	37	7

Table S1. List of reference materials used to check reproducibility and precision during analytical sessions. Data in blue and italics are from Andersen et al. (2015). + Concentrations of U determined from isotope dilution. N.M is the number of individual measurements and N.S is the number of individual samples dissolved and processed through column chromatography.

Sample	BHVO-2	W-2A
Th (ng g^{-1})	1129	2112
Th 2SD	165	401
Th 2SE	14	51
U (ng g^{-1})	383	469
U 2SD	57	85
U 2SE	5	11
Th/U	2.9	4.5
N	147	63
Reference Th (ng g^{-1})	1114	2179
Reference U (ng g^{-1})	386	490
Reference Th/U	2.9	4.4

Table S2. List of reference materials used to check reproducibility and precision of measurements of Th and U concentrations measured on an Element2 ICP-MS. Reference values are from the USGS data sheets.

Section 3:

Ophiolite data and data tables

Sample	Lithology	$\delta^{238}U$ (‰)	2SE	$\delta^{234}U$ (‰)	2SE	U (ng g^{-1})	Th/U	N
Annieopsquotch 480 Ma								
VL01J188	SD	−0.297	0.052	35.4	2.2	34	6.3	3
VL01J189	SD	−0.324	0.049	28.7	2.0	21	4.3	2 (2)
VL01J190	SD	−0.267	0.048	18.7	2.0	97	4.6	2
VL01J191	SD	−0.306	0.023	34.2	0.9	137	4.3	3
VL01J192	SD	−0.498	0.064	25.9	2.7	22	4.7	2
VL01J193	SD	−0.287	0.055	32.5	2.3	19	5.9	2
VL01J194	SD	−0.344	0.052	34.3	2.2	35	4.8	2
VL01J195	Ex	−0.301	0.013	0.0	0.5	187	0.6	6 (2)
VL01J196a	Ex	−0.425	0.036	−9.5	1.5	66	1.7	4 (2)
VL01J196b	Ex	−0.267	0.021	5.3	0.9	49	4.2	4 (2)
VL01J198	Ex	−0.357	0.048	38.7	2.0	33	4.6	2
VL01J199a	Ex	−0.306	0.038	23.5	1.6	40	3.4	2
VL01J199b	Ex	−0.340	0.084	38.5	3.6	11	5.7	1
VL01J200a	Ex	−0.565	0.032	9.3	1.3	80	1.7	5 (2)
VL01J200b	Ex					6	10.0	
VL01J201	Ex	−0.484	0.049	25.3	2.1	61	3.6	3
VL01J202	Ex	−0.335	0.037	7.2	1.5	15	3.5	5 (2)
VL01J203	Ex	−0.300	0.050	23.7	2.1	39	3.2	2
VL01J204a	Ex	−0.399	0.022	11.6	0.9	128	1.4	8 (2)
VL01J204b	Ex	−0.409	0.032	14.5	1.3	76	2.7	5 (2)
VL01J205a	Ex	−0.528	0.027	12.6	1.1	48	2.5	3 (2)
VL01J205b	Ex	−0.356	0.027	−0.2	1.1	89	2.2	6 (2)
Khantaishir 540 Ma								
KT-11-24	G	−0.350	0.080	93.1	3.5	21	1.7	2
KT-11-149	G	−0.287	0.018	−29.1	0.7	164	2.9	2
KT-12-56	G	−0.254	0.057	51.7	2.4	28	2.1	2
KT-12-65	G					2	2.5	
KT-11-157	SDC	−0.293	0.013	−28.7	0.5	336	3.3	5
KTB-4	SDC	−0.201	0.016	1.5	0.6	154	0.8	5 (2)
KTU-4	SDC	−0.471	0.040	4.0	1.7	23	3.1	5 (2)

KT-11-110	SDC	−0.302	0.017	4.9	0.7	89	2.1	6 (2)
KT-11-83	SDC	−0.522	0.028	18.2	1.1	120	0.7	2
KT-11-140	SDC	−0.332	0.026	9.4	1.1	77	1.9	5 (2)
KTU-1	SDC	−0.330	0.023	8.5	0.9	94	2.7	6 (2)
KT-12-78	SDC	−0.321	0.027	21.7	1.1	77	2.0	2
KT-11-70	Ex	−0.399	0.019	442.2	0.7	183	0.6	2
KT-11-85	Ex	−0.496	0.058	183.6	2.4	35	2.1	1
KT-11-86	Ex	−0.238	0.027	38.4	1.1	115	0.7	2
KT-11-87	Ex	−0.590	0.047	61.9	2.0	40	2.5	2
KT-11-96	Ex	−0.338	0.019	9.7	0.7	115	1.6	5 (2)
KTP-1	Ex	−0.404	0.027	21.8	1.1	90	1.0	2
Gabal Gerf 750 Ma								
GG31	U					4	0.4	
GG35	U	−0.087	0.119	97.5	5.4	9	0.4	2
GG68	U	−0.400	0.075	1.5	3.2	19	0.0	2
GG74	U					3	0.2	
GG12	A	−0.261	0.029	26.0	1.2	88	4.4	2
GG257	A	−0.369	0.012	1.7	0.5	464	2.4	5
GG36	G					4	0.7	
GG77	G					10	3.2	
GG79	G	−0.241	0.067	18.7	2.9	16	2.7	2
GG80	G	−0.355	0.107	57.5	4.8	12	1.0	2
GG81	G	−0.199	0.046	9.2	2.0	85	2.8	3
GG82	G	−0.266	0.067	19.2	2.8	17	2.7	2
GG83	G					3	2.8	
GG84	G	−0.288	0.049	18.7	2.0	26	1.7	2
GG85	G	−0.199	0.052	32.0	2.2	25	1.3	2
GG86	G	−0.386	0.064	9.6	2.7	22	2.1	2
GG87	G					14	2.1	
GG88	G					5	3.4	
GG89	G					8	1.8	
GG90	G					8	2.9	
GG91	G					4	3.4	
GG92	G	−0.319	0.047	7.2	2.0	66	2.5	3
GG93	G					5	2.3	
GG71	SD	−0.287	0.022	16.5	0.9	42	2.6	2

GG72	SD	−0.275	0.018	24.9	0.7	44	3.6	2
GG95	SD					9	2.6	
GG170	SD					35	3.3	
GG171	SD					37	3.3	
GG172	SD	−0.208	0.038	40.0	1.5	20	2.0	2
GG173	SD					19	2.1	
GG174	SD	−0.208	0.028	23.9	1.1	39	2.1	2
GG175	SD					16	2.9	
GG176	SD					16	2.8	
GG177	SD					21	2.9	
GG281	SD	−0.244	0.034	7.1	1.4	36	1.8	2
GG9	Ex					87	3.3	
GG10	Ex	−0.250	0.026	1.8	1.0	42	3.1	2
GG13	Ex	−0.325	0.015	−12.4	0.6	304	4.6	3
GG69	Ex					50	3.8	
GG70	Ex					27	3.7	
GG73	Ex	−0.331	0.020	8.6	0.8	42	3.5	2
GG94	Ex					43	3.2	
GG178	Ex	−0.201	0.058	22.3	2.4	16	1.6	2
GG179	Ex	−0.719	0.034	9.3	1.4	22	1.2	2
GG180	Ex	−0.223	0.138	34.5	6.3	16	1.6	2
GG181	Ex					22	3.2	
GG182	Ex	−0.299	0.039	19.6	1.6	22	3.2	2
GG183	Ex					20	2.7	
GG184	Ex	−0.265	0.042	2.4	1.7	28	2.6	2
GG185	Ex					23	3.1	
GG282	Ex	−0.290	0.033	79.1	1.3	23	1.3	2

Table S3. Ophiolite U isotopic data, U concentration data and Th/U ratio data. For samples with measured U isotopic compositions the U concentrations have been calculated by isotope dilution. All Th concentration data and U concentration data for samples with no U isotopic data were acquired on an Element2 ICP-MS at the University of Bristol. N refers to the number of individual measurements and values in brackets the number of individual digestions and columns processed, 2SE is calculated from the method described in the Supplementary Material: Section 2. Lithology abbreviations: U = Ultramafic, A = Amphibolite, G = Gabbro, SD = Sheeted dyke, SDC = Sill and dyke complex, Ex = Extrusive section. Groupings have been made according to sample descriptions found in literature. In some cases such as for sill and dyke complex samples and sheeted dykes samples, they can crosscut into other units; in these cases, the samples have been grouped still as part of the sill and dyke complex and sheeted dykes. Samples highlighted in green are those that show clear signs of U enrichment (see main text for details).

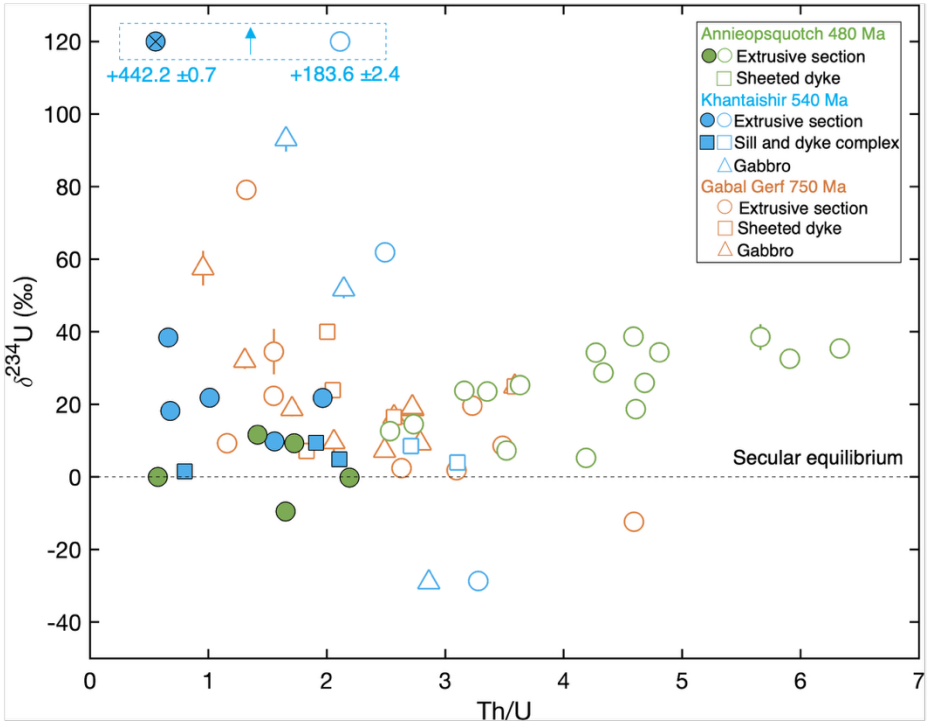

Fig. S4. (a) $\delta^{234}U$ vs. Th/U. Dashed black line at $\delta^{234}U = 0$ represents secular equilibrium. Samples from Khantaishir circled in the dashed blue box plot off the scale in $\delta^{234}U$ (Table S3). Error bars are 2SE.

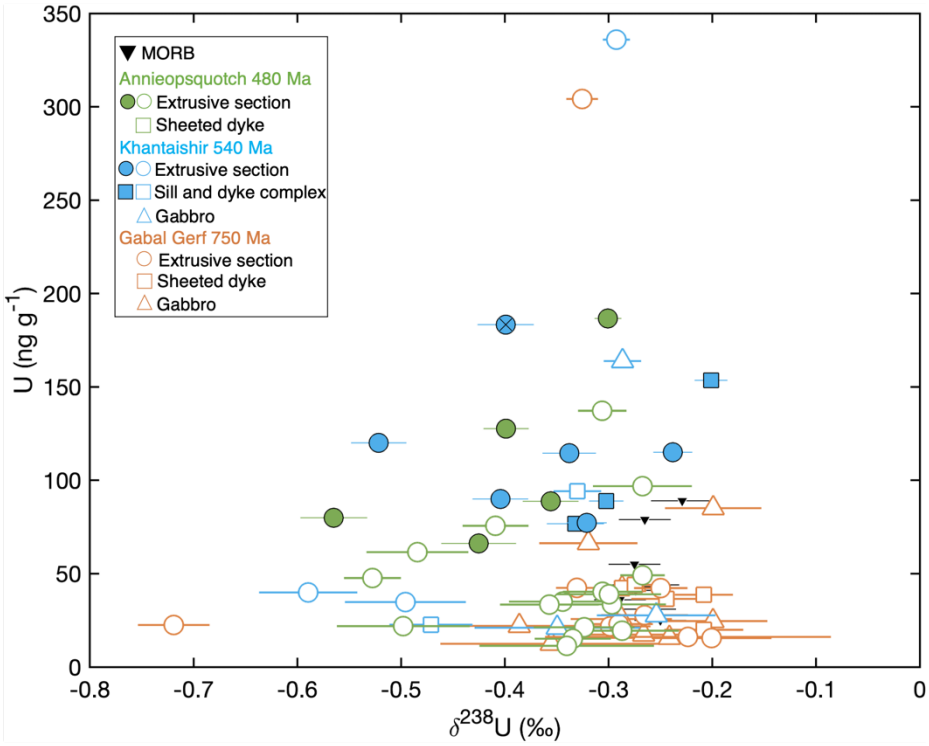

Fig. S5. Uranium concentration vs. $\delta^{238}U$. Samples of MORB (black inverted triangles) are from Andersen et al. (2015). Error bars are 2SE.

Section 4:

Recent U addition from a groundwater source modelling

We can estimate the potential impact of recent sub-aerial U uptake on $\delta^{238}U$ compositions by assuming that the $\delta^{234}U$ compositions of samples with $\delta^{234}U > 0$ is a mixture between recent U uptake from a groundwater fluid with an assumed high $\delta^{234}U$ and older (>2 Ma) U with $\delta^{234}U = 0$. We take the approach of Andersen et al. (2024) and assume a $\delta^{234}U$ for the fluid adding U of +1000 % (Osmond and Cowart, 1976). Using this mixture between recent added U and older U we calculate the fraction of U in samples that was added recently (Table S4). This estimate shows generally low amounts of recently added U (<10 %), but for some samples in Khantaishir ranges up to ~ 44 %. Removing this recent added U from samples results in minimal change in Th/U ratios of most samples (Fig. S6a), especially those with $\delta^{234}U$ closest to secular equilibrium and the most enriched in U, with the largest change in sample KT-11-70 ($\delta^{234}U$ = +442 ‰). We also apply the same correction to $\delta^{238}U$ values by assuming the fluid adding recent U has a $\delta^{238}U$ compositions of the highest and lowest $\delta^{238}U$ composition in each ophiolite. Again, most samples show minimal change in $\delta^{238}U$ (<0.1 ‰) and are generally within analytical uncertainty (Fig. S6b & c), especially for samples that show the most U enrichment. This is however bar sample KT-11-70 (marked with a x on Fig. 2, 3, S4, S5, and S6) which shows the largest change outside of uncertainty.

Sample	Lithology	$\delta^{238}U$ (‰)	$\delta^{234}U$ (‰)	U (ng g^{-1})	Th/U	Fraction U added	Added U (ng g^{-1})	Th/U Corrected	$\delta^{238}U$ (‰) Corrected[a]	$\delta^{238}U$ (‰) Corrected[b]
Annieopsquotch 480 Ma										
VL01J188	SD	−0.297	35.4	34	6.3	0.04	1.2	6.6	−0.287	−0.298
VL01J189	SD	−0.324	28.7	21	4.3	0.03	0.6	4.5	−0.316	−0.325
VL01J190	SD	−0.267	18.7	97	4.6	0.02	1.8	4.7	−0.262	−0.267
VL01J191	SD	−0.306	34.2	137	4.3	0.03	4.7	4.4	−0.297	−0.307
VL01J192	SD	−0.498	25.9	22	4.7	0.03	0.6	4.8	−0.496	−0.504
VL01J193	SD	−0.287	32.5	19	5.9	0.03	0.6	6.1	−0.278	−0.288
VL01J194	SD	−0.344	34.3	35	4.8	0.03	1.2	5.0	−0.336	−0.347
VL01J195	Ex	−0.301	0.0	187	0.6	0.00	0.0	0.6	−0.301	−0.301
VL01J196a	Ex	−0.425	−9.5	66	1.7					
VL01J196b	Ex	−0.267	5.3	49	4.2	0.01	0.3	4.2	−0.266	−0.267
VL01J198	Ex	−0.357	38.7	33	4.6	0.04	1.3	4.8	−0.349	−0.361
VL01J199a	Ex	−0.306	23.5	40	3.4	0.02	0.9	3.4	−0.300	−0.307
VL01J199b	Ex	−0.340	38.5	11	5.7	0.04	0.4	5.9	−0.331	−0.343
VL01J200a	Ex	−0.565	9.3	80	1.7	0.01	0.7	1.7	−0.565	−0.568
VL01J200b	Ex			6	10.0					
VL01J201	Ex	−0.484	25.3	61	3.6	0.03	1.6	3.7	−0.482	−0.490
VL01J202	Ex	−0.335	7.2	15	3.5	0.01	0.1	3.5	−0.333	−0.335
VL01J203	Ex	−0.300	23.7	39	3.2	0.02	0.9	3.2	−0.293	−0.300
VL01J204a	Ex	−0.399	11.6	128	1.4	0.01	1.5	1.4	−0.397	−0.400
VL01J204b	Ex	−0.409	14.5	76	2.7	0.01	1.1	2.8	−0.407	−0.411
VL01J205a	Ex	−0.528	12.6	48	2.5	0.01	0.6	2.6	−0.527	−0.531
VL01J205b	Ex	−0.356	−0.2	89	2.2					
Khantaishir 540 Ma										
KT-11-24	G	−0.350	93.1	21	1.7	0.09	2.0	1.8	−0.325	−0.365
KT-11-149	G	−0.287	−29.1	164	2.9					
KT-12-56	G	−0.254	51.7	28	2.1	0.05	1.4	2.3	−0.236	−0.257
KT-12-65	G			2	2.5					
KT-11-157	SDC	−0.293	−28.7	336	3.3					
KTB-4	SDC	−0.201	1.5	154	0.8	0.00	0.2	0.8	−0.201	−0.201
KTU-4	SDC	−0.471	4.0	23	3.1	0.00	0.1	3.1	−0.471	−0.472
KT-11-110	SDC	−0.302	4.9	89	2.1	0.00	0.4	2.1	−0.301	−0.303
KT-11-83	SDC	−0.522	18.2	120	0.7	0.02	2.2	0.7	−0.520	−0.527
KT-11-140	SDC	−0.332	9.4	77	1.9	0.01	0.7	1.9	−0.330	−0.333
KTU-1	SDC	−0.330	8.5	94	2.7	0.01	0.8	2.7	−0.328	−0.331
KT-12-78	SDC	−0.321	21.7	77	2.0	0.02	1.7	2.0	−0.315	−0.324
KT-11-70	Ex	−0.399	442.2	183	0.6	0.44	81.1	1.0	−0.248	−0.556
KT-11-85	Ex	−0.496	183.6	35	2.1	0.18	6.4	2.6	−0.475	−0.562
KT-11-86	Ex	−0.238	38.4	115	0.7	0.04	4.4	0.7	−0.224	−0.240
KT-11-87	Ex	−0.590	61.9	40	2.5	0.06	2.5	2.7	−0.590	−0.615
KT-11-96	Ex	−0.338	9.7	115	1.6	0.01	1.1	1.6	−0.335	−0.339
KTP-1	Ex	−0.404	21.8	90	1.0	0.02	2.0	1.0	−0.400	−0.409
Gabal Gerf 750 Ma										
GG31	U			4	0.4					
GG35	U	−0.087	97.5	9	0.4					
GG68	U	−0.400	1.5	19	0.0					
GG74	U			3	0.2					
GG12	A	−0.261	26.0	88	4.4					
GG257	A	−0.369	1.7	464	2.4					
GG36	G			4	0.7					
GG77	G			10	3.2					
GG79	G	−0.241	18.7	16	2.7	0.02	0.3	2.8	−0.232	−0.242
GG80	G	−0.355	57.5	12	1.0	0.06	0.7	1.0	−0.333	−0.365
GG81	G	−0.199	9.2	85	2.8	0.01	0.8	2.8	−0.194	−0.199
GG82	G	−0.266	19.2	17	2.7	0.02	0.3	2.8	−0.257	−0.267

GG83	G			3	2.8					
GG84	G	−0.288	18.7	26	1.7	0.02	0.5	1.7	−0.279	−0.289
GG85	G	−0.199	32.0	25	1.3	0.03	0.8	1.3	−0.182	−0.199
GG86	G	−0.386	9.6	22	2.1	0.01	0.2	2.1	−0.383	−0.388
GG87	G			14	2.1					
GG88	G			5	3.4					
GG89	G			8	1.8					
GG90	G			8	2.9					
GG91	G			4	3.4					
GG92	G	−0.319	7.2	66	2.5	0.01	0.5	2.5	−0.317	−0.320
GG93	G			5	2.3					
GG71	SD	−0.287	16.5	42	2.6	0.02	0.7	2.6	−0.280	−0.288
GG72	SD	−0.275	24.9	44	3.6	0.02	1.1	3.7	−0.263	−0.277
GG95	SD			9	2.6					
GG170	SD			35	3.3					
GG171	SD			37	3.3					
GG172	SD	−0.208	40.0	20	2.0	0.04	0.8	2.1	−0.187	−0.209
GG173	SD			19	2.1					
GG174	SD	−0.208	23.9	39	2.1	0.02	0.9	2.1	−0.196	−0.208
GG175	SD			16	2.9					
GG176	SD			16	2.8					
GG177	SD			21	2.9					
GG281	SD	−0.244	7.1	36	1.8	0.01	0.3	1.8	−0.241	−0.245
GG9	Ex			87	3.3					
GG10	Ex	−0.250	1.8	42	3.1	0.00	0.1	3.1	−0.249	−0.250
GG13	Ex	−0.325	−12.4	304	4.6					
GG69	Ex			50	3.8					
GG70	Ex			27	3.7					
GG73	Ex	−0.331	8.6	42	3.5	0.01	0.4	3.5	−0.327	−0.332
GG94	Ex			43	3.2					
GG178	Ex	−0.201	22.3	16	1.6	0.02	0.3	1.6	−0.189	−0.201
GG179	Ex	−0.719	9.3	22	1.2	0.01	0.2	1.2	−0.719	−0.724
GG180	Ex	−0.223	34.5	16	1.6	0.03	0.6	1.6	−0.206	−0.224
GG181	Ex			22	3.2					
GG182	Ex	−0.299	19.6	22	3.2	0.02	0.4	3.3	−0.290	−0.300
GG183	Ex			20	2.7					
GG184	Ex	−0.265	2.4	28	2.6	0.00	0.1	2.6	−0.264	−0.265
GG185	Ex			23	3.1					
GG282	Ex	−0.290	79.1	23	1.3	0.08	1.8	1.4	−0.254	−0.298

Table S4. Ophiolite samples corrected for a recent flux of groundwater U addition, using an estimated groundwater composition of $\delta^{234}U$ = 1000 ‰. Readers are referred to the online version of the supplementary data tables for calculations. a – Samples corrected in $\delta^{238}U$ using lowest $\delta^{238}U$ in each ophiolite, b – Samples corrected in $\delta^{238}U$ using highest $\delta^{238}U$ in each ophiolite.

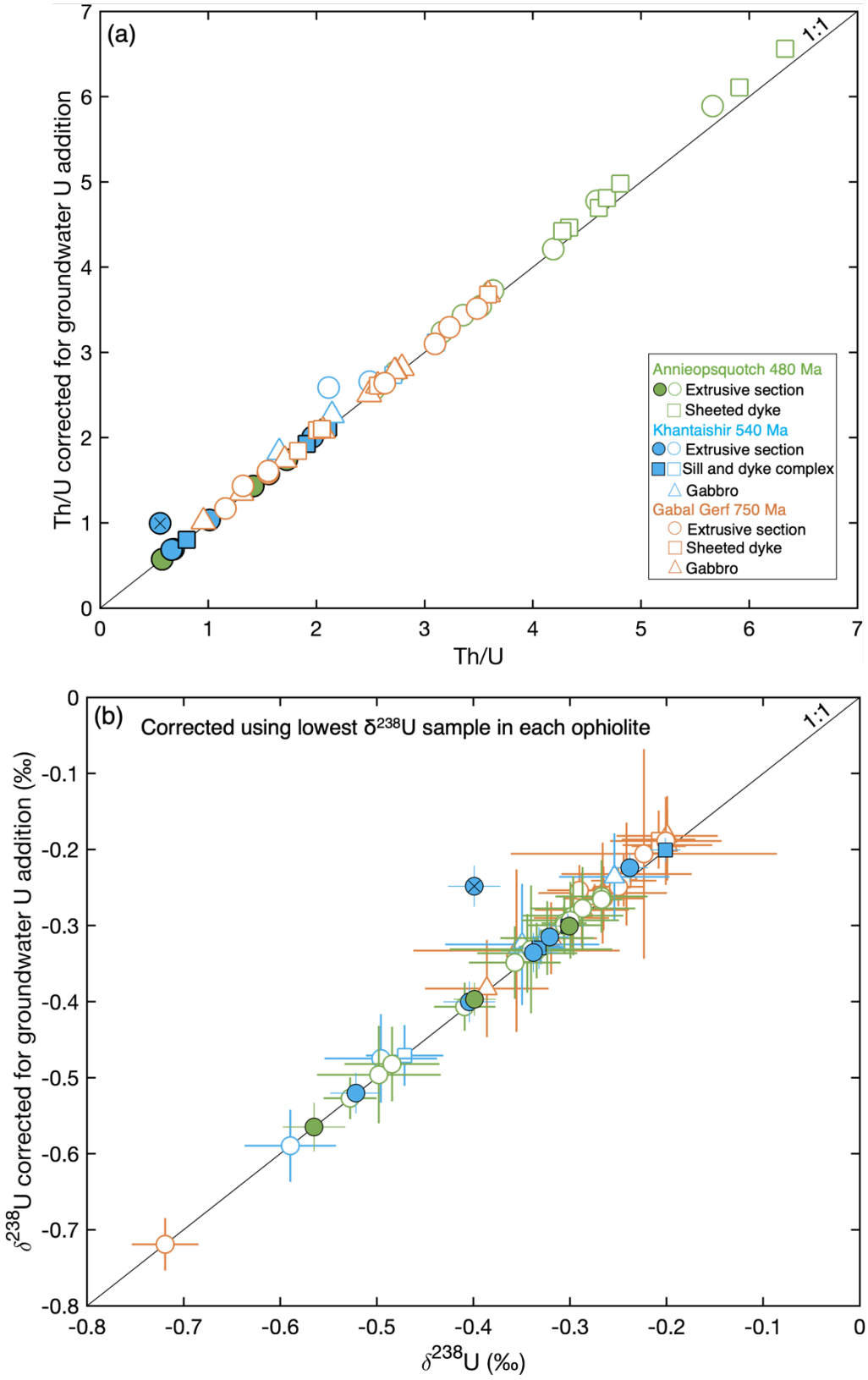
(a)
1:1
Th/U corrected for groundwater U addition
Th/U
Annieopsquotch 480 Ma
Extrusive section
Sheeted dyke
Khantaishir 540 Ma
Extrusive section
Sill and dyke complex
Gabbro
Gabal Gerf 750 Ma
Extrusive section
Sheeted dyke
Gabbro
(b)
Corrected using lowest δ238U sample in each ophiolite
1:1
δ238U corrected for groundwater U addition (‰)
δ238U (‰)

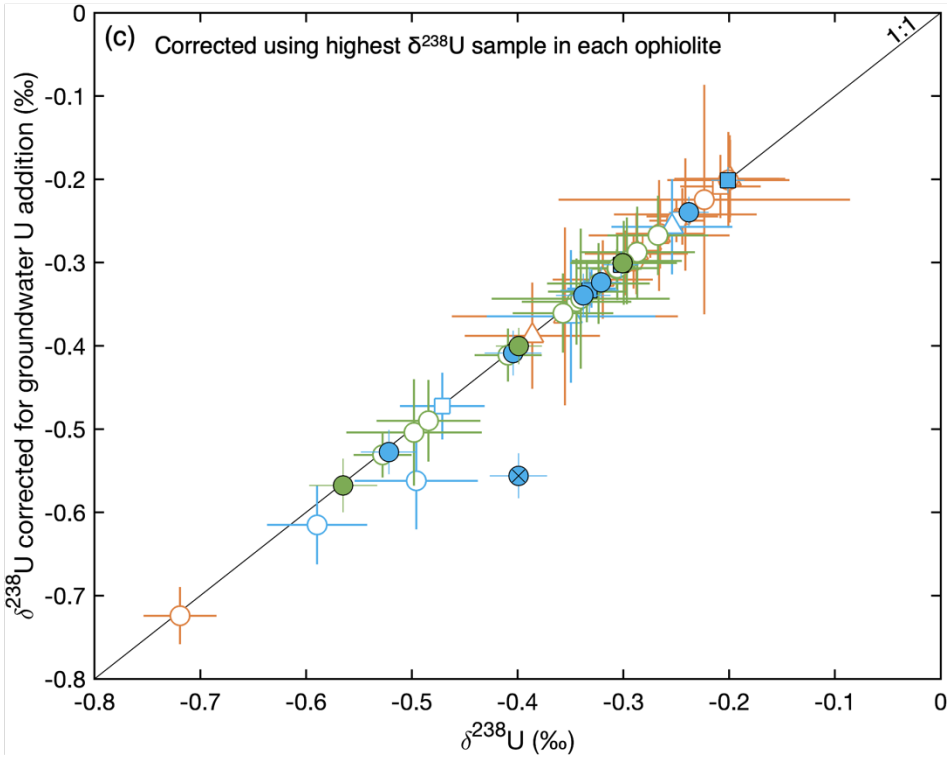

Fig. S6. (a) Th/U and (b & c) δ^{238}U composition of ophiolite samples corrected for recent U addition from a groundwater source versus measured compositions, see Supplementary Material Section: 4 for details of modelling. The black diagonal line represents the 1:1 line. In (b) data are corrected using the lowest δ^{238}U composition in each respective ophiolite and in (c) the highest δ^{238}U composition. Error bars are 2SE.

Section 5:

Iron systematics

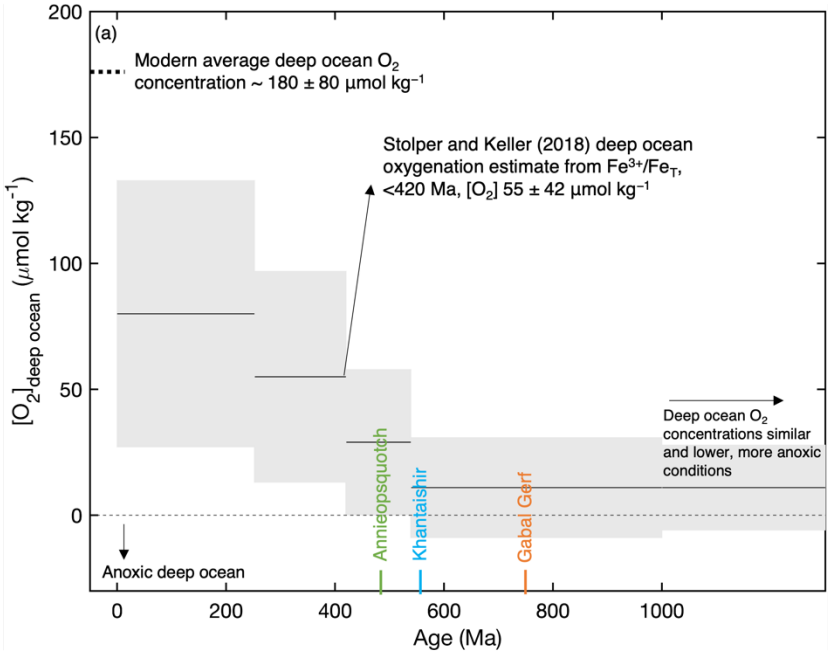

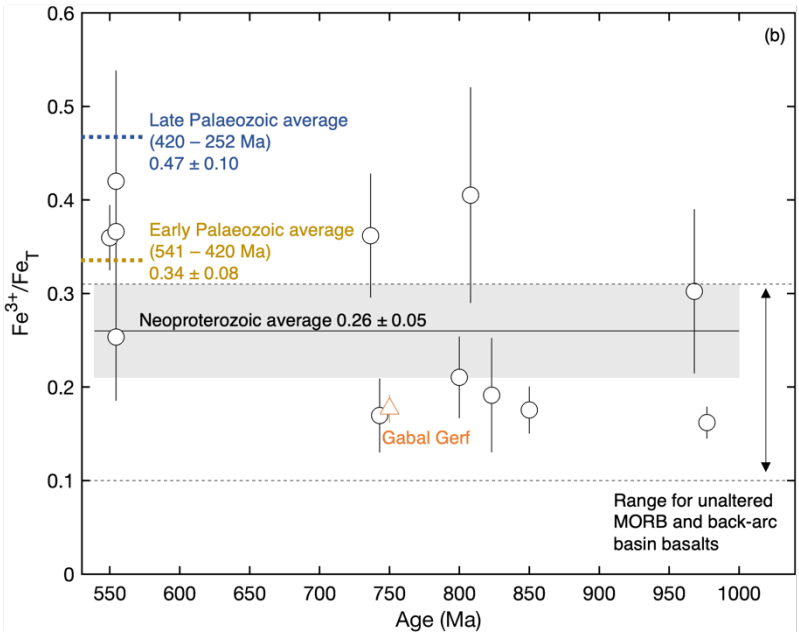

Fig. S7. (a) Modelled deep ocean O_2 concentrations over time from Stolper and Keller (2018) calculated from increases in Fe^{3+}/Fe_T observed in ophiolites relative to unaltered MORB. Thin black lines represent averages and grey shaded region the 2SE. Dotted black line at the top left indicates the O_2 concentration level of modern deep oceans from Sarmiento and Gruber (2006). Figure is based on figure 4a from Stolper and Keller (2018). (b) Iron data for Neoproterozoic ophiolites in the compilation from Stolper and Keller (2018). Data for all Gabal Gerf samples are shown bar the peridotite and amphibolite samples, including samples not measured for $\delta^{238}U$. Error bars are 2SE.

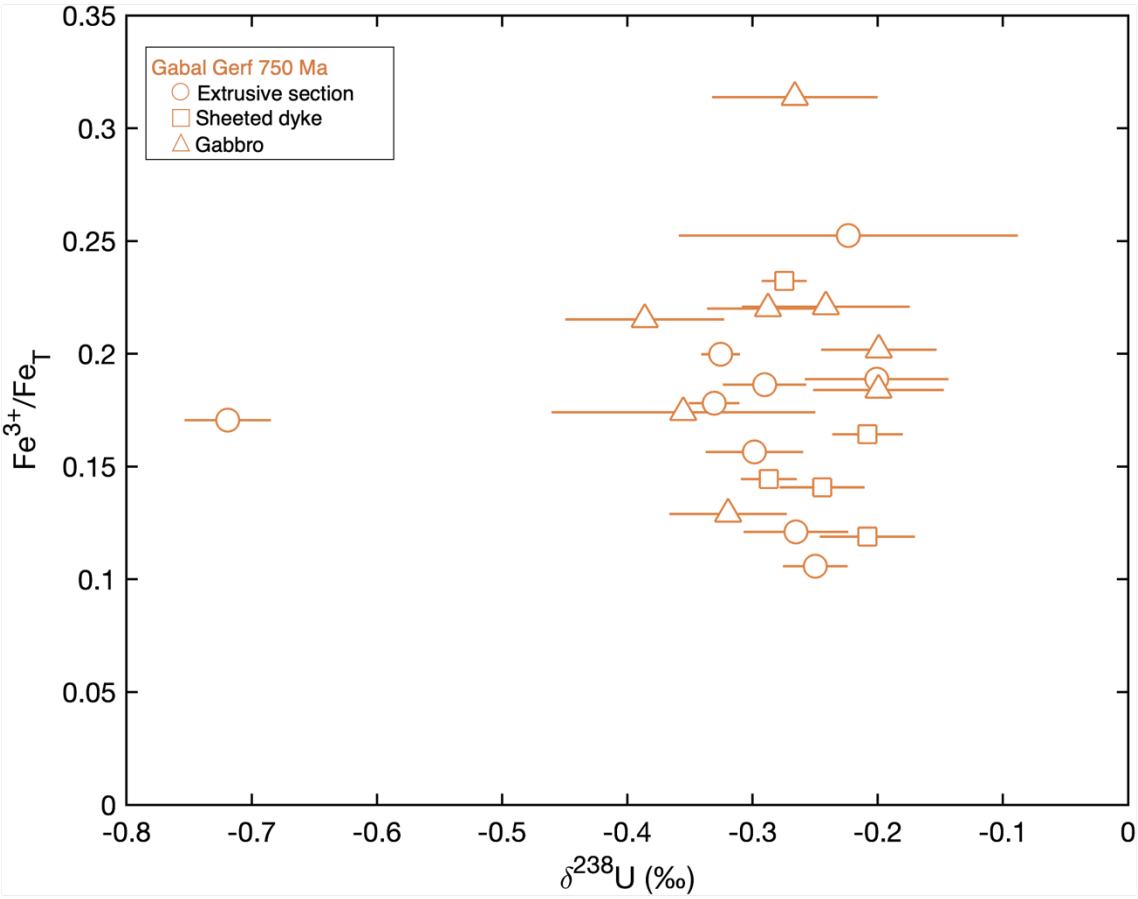

Fig. S8. Variation in Fe^{3+}/Fe_T vs. $\delta^{238}U$ for Gabal Gerf samples. Iron data is from Zimmer et al. (1995). Error bars are 2SE.

References

Alt, J. C., C. Laverne, R. M. Coggon, D. A. H. Teagle, N. R. Banerjee, S. Morgan, C. E. Smith-Duque, M. Harris, and L. Galli, 2010, Subsurface structure of a submarine hydrothermal system in ocean crust formed at the East Pacific Rise, ODP/IODP Site 1256: Submarine hydrothermal system: Geochemistry, Geophysics, Geosystems, **11**, Q10010.

Andersen, M. B., S. Romaniello, D. Vance, S. H. Little, R. Herdman, and T. W. Lyons, 2014, A modern framework for the interpretation of $^{238}U/^{235}U$ in studies of ancient ocean redox: Earth and Planetary Science Letters, **400**, 184–194.

Andersen, M. B., T. Elliott, H. Freymuth, K. W. W. Sims, Y. Niu, and K. A. Kelley, 2015, The terrestrial uranium isotope cycle: Nature, **517**, 356–359.

Andersen, M. B., J. B. Rodney, H. Freymuth, F. Vils, M. Harris, K. Cooper, D. A. H. Teagle, and T. Elliott, 2024, Time scales and mechanisms of uranium uptake in altered ocean crust; observations from the ~15 million year-old site 1256 in the eastern equatorial Pacific: Geochimica et Cosmochimica Acta, **382**, 142–159.

Bach, W., B. Peucker-Ehrenbrink, S. R. Hart, and J. S. Blusztajn, 2003, Geochemistry of hydrothermally altered oceanic crust: DSDP/ODP Hole 504B - Implications for seawater-crust exchange budgets and Sr- and Pb-isotopic evolution of the mantle: Hydrothermally altered oceanic crust: Geochemistry, Geophysics, Geosystems, **4**, 8904.

Cheng, H., R. Lawrence Edwards, C.-C. Shen, V. J. Polyak, Y. Asmerom, J. Woodhead, J. Hellstrom, Y. Wang, X. Kong, C. Spötl, X. Wang, and E. Calvin Alexander, 2013, Improvements in ^{230}Th dating, ^{230}Th and ^{234}U half-life values, and U–Th isotopic measurements by multi-collector inductively coupled plasma mass spectrometry: Earth and Planetary Science Letters, **371–372**, 82–91.

Condon, D. J., N. McLean, S. R. Noble, and S. A. Bowring, 2010, Isotopic composition ($^{238}U/^{235}U$) of some commonly used uranium reference materials: Geochimica et Cosmochimica Acta, **74**, 7127–7143.

Dilek, Y., and H. Furnes, 2011, Ophiolite genesis and global tectonics: Geochemical and tectonic fingerprinting of ancient oceanic lithosphere: Geological Society of America Bulletin, **123**, 387–411.

Gale, A., C. A. Dalton, C. H. Langmuir, Y. Su, and J.-G. Schilling, 2013, The mean composition of ocean ridge basalts: Geochemistry, Geophysics, Geosystems, **14**, 489–518.

Gianola, O., M. W. Schmidt, O. Jagoutz, J. Rickli, O. Bruguier, and O. Sambuu, 2019, The Crust–Mantle Transition of the Khantaishir Arc Ophiolite (Western Mongolia): Journal of Petrology, **60**, 673–700.

Hiess, J., D. J. Condon, N. McLean, and S. R. Noble, 2012, $^{238}U/^{235}U$ Systematics in Terrestrial Uranium-Bearing Minerals: Science, **335**, 1610–1614.

Kelley, K., T. Plank, L. Farr, J. Ludden, and H. Staudigel, 2005, Subduction cycling of U, Th, and Pb: Earth and Planetary Science Letters, **234**, 369–383.

Lissenberg, C. J., C. R. van Staal, J. H. Bédard, and A. Zagorevski, 2005, Geochemical constraints on the origin of the Annieopsquotch ophiolite belt, Newfoundland Appalachians: Geological Society of America Bulletin, **117**, 1413.

Osmond, J. K., and J. B. Cowart, 1976, The theory and uses of natural uranium isotopic variations in hydrology: Atomic Energy Review, **14**, 621–679.

Richter, S., A. Alonso-Munoz, R. Eykens, U. Jacobsson, H. Kuehn, A. Verbruggen, Y. Aregbe, R. Wellum, and E. Keegan, 2008, The isotopic composition of natural uranium samples - Measurements using the new n(^{233}U)/n(^{236}U) double spike IRMM-3636: International Journal of Mass Spectrometry, **269**, 145–148.

Sarmiento, J. L., and N. Gruber, 2006, Ocean Biogeochemical Dynamics: Princeton University Press.

Staudigel, H., T. Plank, B. White, and H.-U. Schmincke, 1996, Geochemical Fluxes During Seafloor Alteration of the Basaltic Upper Oceanic Crust: DSDP Sites 417 and 418, *in* Subduction, American Geophysical Union (AGU), 19–38.

Stolper, D. A., and C. B. Keller, 2018, A record of deep-ocean dissolved O2 from the oxidation state of iron in submarine basalts: Nature, **553**, 323–327.

Zimmer, M., A. Kröner, K. P. Jochum, T. Reischmann, and W. Todt, 1995, The Gabal Gerf complex: A precambrian N-MORB ophiolite in the Nubian Shield, NE Africa: Chemical Geology, **123**, 29–51.